

Available energy of trapped electrons in Miller tokamak equilibria

R.J.J. Mackenbach^{1,2}†, J.H.E. Proll¹, G. Snoep^{1,3}, and P. Helander²

¹Eindhoven University of Technology, 5612 AZ Eindhoven, The Netherlands

²Max Planck Institute for Plasma Physics, 17491 Greifswald, Germany

³DIFFER - Dutch Institute for Fundamental Energy Research, Eindhoven, The Netherlands

(Received xx; revised xx; accepted xx)

Available energy (\mathcal{A}), which quantifies the maximum amount of thermal energy that may be liberated and converted into instabilities and turbulence, has shown to be a useful metric for predicting saturated energy fluxes in trapped-electron-mode-driven turbulence. Here, we calculate and investigate the \mathcal{A} in the analytical tokamak equilibria introduced by Miller *et al.* (1998). The \mathcal{A} of trapped electrons reproduces various trends also observed in experiments; negative shear, increasing Shafranov shift, and negative triangularity can all be stabilising as indicated by a reduction in \mathcal{A} , though it is strongly dependent on the chosen equilibrium. We find that negative triangularity is especially beneficial in vertically elongated configurations with positive shear, or low gradients. We furthermore extract a gradient-threshold like quantity from \mathcal{A} and find that it behaves similarly to gyrokinetic gradient-thresholds: it tends to increase linearly with magnetic shear, and negative triangularity leads to an especially high threshold. We next optimise device geometry for minimal \mathcal{A} and find that the optimum is strongly dependent on equilibrium parameters, e.g. magnetic shear or pressure gradient. If one furthermore investigates the competing effects of increasing the density gradient, pressure gradient, and decreasing the shear, one finds regimes which have steep gradients yet low \mathcal{A} , and that such a regime is inaccessible in negative-triangularity tokamaks. We finally compare \mathcal{A} with saturated heat-flux estimates from the TGLF model and find fairly good correspondence.

1. Introduction

Transport in tokamaks and stellarators is largely dominated by turbulent energy losses, which severely degrade the energy confinement in these devices. A detailed understanding of how various parameters characterising the plasma and the magnetic-field geometry, such as magnetic shear and the pressure gradient, affect the turbulent transport properties would be helpful for comprehending and mitigating it. The standard method to assess the turbulence properties of any given tokamak is to perform nonlinear gyrokinetic simulations. However, such simulations are computationally expensive because of the very disparate time- and length scales characterising the turbulence and the transport. It would thus be beneficial to find a reduced model capable of predicting the level of turbulent transport by simpler means.

In a recent publication, it was shown that the available energy (\mathcal{A}) of trapped electrons can serve as such a reduced model (Mackenbach *et al.* 2022), at least for turbulence driven by the plasma density gradient. Any plasma possesses a maximum amount of thermal energy that can be converted into instabilities and turbulence (Gardner 1963). This “available” energy can be calculated by performing a Gardner restacking of the

† Email address for correspondence: r.j.j.mackenbach@tue.nl

plasma distribution function f , in which phase-space volume elements are rearranged in a manner that respects Liouville's theorem (Kolmes *et al.* 2020; Kolmes & Fisch 2020). The restacking of f which minimizes the thermal energy results in a “ground state” distribution function f_g , and the \mathcal{AE} is defined as the difference in thermal energy between f and f_g . If one imposes the additional constraint that adiabatic invariants be conserved in the restacking process, the \mathcal{AE} becomes relevant to magnetically confined plasmas (Helander 2017, 2020). In fusion plasmas, the magnetic moment μ is usually conserved for all species, and the parallel adiabatic invariant $\mathcal{J} = \int mv_{\parallel} d\ell$ is conserved for magnetically trapped electrons.

A significant portion of electrons are trapped, and can contribute to the turbulence through trapped electron modes (TEMs). The \mathcal{AE} of trapped electrons correlates with the turbulent energy flux for such TEM-driven turbulence over several orders of magnitude in saturated energy fluxes (Mackenbach *et al.* 2022). This correlation is expressible as a simple power law, where the saturated energy flux, Q_{sat} , was found to be related to the available energy, which we denote by A in formulas, via approximately

$$Q_{\text{sat}} \propto A^{3/2}. \quad (1.1)$$

This relation was found to hold for both a tokamak and stellarators, and for various values of the density gradient. Aside from this relationship, other links have been found by Kolmes & Fisch (2022) where quasi-linear plateauing is shown to be related to a concept closely connected to \mathcal{AE} , highlighting other links to transport physics. In any case, in order to gain a deeper understanding it is of interest to derive an explicit expression of the \mathcal{AE} in tokamak geometry, in order to investigate the dependence of \mathcal{AE} on various geometrical and plasma parameters.

This is our aim in the present paper, where we compute the \mathcal{AE} for the family of tokamak equilibria constructed by Miller *et al.* (1998). The starting point is the following explicit expression for the \mathcal{AE} on a flux surface of any omnigenous equilibrium (Helander 2020; Mackenbach *et al.* 2023b), including that of a tokamak,

$$A = \frac{1}{2\sqrt{\pi}} \frac{\pi L \Delta\psi_t \Delta\alpha}{B_0} \iint_{\text{wells}} \sum e^{-z} z^{5/2} \hat{\omega}_{\alpha}^2 \mathcal{R} \left[\frac{1}{z} \frac{\hat{\omega}_{\alpha}^T}{\hat{\omega}_{\alpha}} - 1 \right] \hat{g}^{1/2} d\lambda dz, \quad (1.2)$$

Here, L is the total length of a field-line completing one poloidal turn, B_0 is some reference magnetic field strength, $z = H/T_0$ is the particle energy normalized by the temperature, $\lambda = \mu B_0 / H$ is the pitch angle, and $\Delta\psi_t$ and $\Delta\alpha$ denote the size of the flux-tube in the radial and binormal directions respectively (we have parameterized the radial coordinate by means of the toroidal flux ψ_t and the binormal by means of the Clebsch angle α). The hatted quantities in the integrand denote normalized frequencies, with $\hat{\omega}_{\alpha}$ being the normalized bounce-averaged drift precession frequency, $\hat{\omega}_{\alpha}^T$ the normalized electron diamagnetic drift frequency, and $\hat{g}^{1/2}$ the normalized bounce-time. They are explicitly defined as

$$\hat{\omega}_{\alpha} \equiv -\frac{\Delta\psi_t}{H} \frac{\partial_{\psi_t} \mathcal{J}}{\partial_H \mathcal{J}} \quad (1.3a)$$

$$\hat{\omega}_{\alpha}^T \equiv \Delta\psi_t \frac{d \ln n}{d\psi_t} \left(1 + \eta \left[z - \frac{3}{2} \right] \right) \quad (1.3b)$$

$$\hat{g}^{1/2} \equiv \frac{\partial_H \mathcal{J}}{L} \sqrt{\frac{2H}{m}} \quad (1.3c)$$

where we have denoted the ratio between the gradients by $\eta = (d \ln T / d\psi_t) / (d \ln n / d\psi_t)$.

Finally, $\mathcal{R}[x] = (x + |x|)/2$ is the ramp function. Using the above expressions, we shall find the \mathcal{A} of any Miller tokamak.

2. Theory

2.1. The available energy in any omnigenous systems

We first note that the integral over z can be rewritten into a convenient form. We define two functions which are independent of z , namely

$$c_0 = -\frac{\Delta\psi_t}{\hat{\omega}_\alpha(\lambda)} \frac{d\ln(n)}{d\psi_t} \left(1 - \frac{3}{2}\eta\right), \quad c_1 = 1 + \frac{\Delta\psi_t}{\hat{\omega}_\alpha(\lambda)} \frac{d\ln(n)}{d\psi_t} \eta. \quad (2.1)$$

With these functions, the integral over the normalized energy z reduces to the following form,

$$I_z(c_0, c_1) = \frac{8}{3\sqrt{\pi}} \int_0^\infty \exp(-z) z^{3/2} \mathcal{R}[c_0 - c_1 z] dz. \quad (2.2)$$

This integral can be solved analytically and its functional form depends on the signs of c_0 and c_1 , resulting in four different conditions. The easiest case to evaluate is the case where $c_0 < 0$ and $c_1 > 0$. In this case the argument of the ramp function is always negative, and hence the integral reduces to zero. The second case is when the argument of the ramp function is always positive, which happens whenever $c_0 \geq 0$ and $c_1 \leq 0$. The integral then reduces to the following form

$$I_z = 2c_0 - 5c_1. \quad (2.3)$$

There are two cases left to consider. Firstly we inspect the case where the argument of the ramp function is positive for low z but becomes negative for high z , i.e. $c_0 \geq 0$ and $c_1 > 0$. The unique point where the argument of the ramp function vanishes is

$$z_* = \frac{c_0}{c_1}. \quad (2.4)$$

Thus the integral becomes

$$I_z = \frac{8}{3\sqrt{\pi}} \int_0^{z_*} \exp(-z) z^{3/2} (c_0 - c_1 z) dz. \quad (2.5)$$

This integral can be expressed in terms of the error function, $\text{erf}(x) = 2/\sqrt{\pi} \int_0^x \exp(-t^2) dt$,

$$I_z = (2c_0 - 5c_1) \text{erf} \left(\sqrt{\frac{c_0}{c_1}} \right) + \frac{2}{3\sqrt{\pi}} (4c_0 + 15c_1) \sqrt{\frac{c_0}{c_1}} \exp \left(-\frac{c_0}{c_1} \right). \quad (2.6)$$

The final case is that where the argument of the ramp function is negative for low z but becomes positive for high z , i.e. $c_0 < 0$ and $c_1 \leq 0$. The integral then becomes,

$$I_z = (2c_0 - 5c_1) \left[1 - \text{erf} \left(\sqrt{\frac{c_0}{c_1}} \right) \right] - \frac{2}{3\sqrt{\pi}} (4c_0 + 15c_1) \sqrt{\frac{c_0}{c_1}} \exp \left(-\frac{c_0}{c_1} \right). \quad (2.7)$$

Note that $I_z \geq 0$, $\forall (c_0, c_1) \in \mathbb{R}^2$, which can also be seen in Fig. 1. The \mathcal{A} can now be found by executing the integral over the remaining coordinate

$$A = \frac{3}{16} \frac{\Delta\psi_t \Delta\alpha L}{B_0} n_0 T_0 \int_{\{\lambda\}} d\lambda \sum_{\text{wells}(\lambda)} I_z(c_0, c_1) \hat{\omega}_\alpha^2 \hat{g}^{1/2}. \quad (2.8)$$

Note that this expression is completely general; no approximations have been made in executing these integrals, aside from the preceding assumption of omnigenicity.

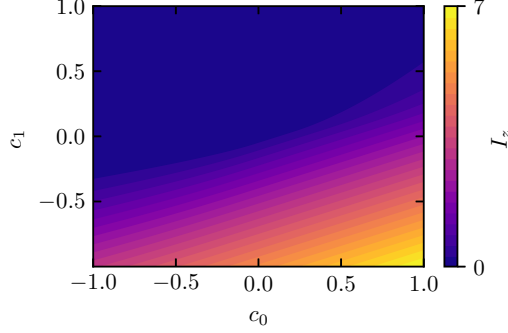


Figure 1: Contour plot of I_z as a function of c_0 and c_1 .

It is also interesting to note that from this expression, one can see that there are no tokamak configurations with vanishing \mathcal{E} , at least to leading order near the axis. This conclusion can most readily be drawn by investigating the expression for ω_α from Connor *et al.* (1983). Here, one can find that there is always a zero-crossing for ω_α , implying that c_0 and c_1 must change sign. As such, the available energy *must* be non-zero (as either $I(c_0, c_1)$ or $I(-c_0, -c_1)$ must be non-zero). Formally, this corresponds to the fact that such a zero-crossing implies that the device does not have the so-called maximum- \mathcal{J} property, which is required for the linear stability of trapped electron modes.

To make further progress in solving Eq. (2.8), one requires the function $\hat{\omega}_\alpha(\lambda)$, which in turn necessitates a specification of the equilibrium. In this paper, we will make use of local construction of the equilibrium, employing a formalism developed by C. Mercier & N. Luc (1974).

2.2. Construction of local equilibria

Equilibria are constructed by finding a radially local solution to the Grad-Shafranov equation, and this solution allows us to find $\hat{\omega}_\alpha$. We highlight the essential components of this derivation, which essentially follows steps taken by Miller *et al.* (1998).

The Luc-Mercier formalism requires the shape of the flux surface, the poloidal field B_p on that flux surface, and the gradients of the pressure $p(\psi)$ and the toroidal field function $f(\psi) = RB_\phi$ on the flux surface, where R is the major radial coordinate, B_ϕ is the toroidal component of the magnetic field, and ψ is the poloidal flux. We parameterize the flux-surface as $R_s = R_s(l)$ and $Z_s = Z_s(l)$, where l measures the poloidal arclength along the flux surface. It is furthermore useful to define a tangential angle u , which measures the angle between the unit vector in the major radial direction e_R and the vector tangential to the flux surface e_l in a clockwise manner, thus

$$\frac{dR_s(l)}{dl} = \cos u, \quad (2.9a)$$

$$\frac{dZ_s(l)}{dl} = -\sin u. \quad (2.9b)$$

With this definition, the angle u can be calculated by $du/dl = -1/R_c$, where $R_c(l)$ is the radius of curvature of the poloidal cross-section, and the negative sign arises because the poloidal arclength is measured clockwise. We go on to introduce a radial-like expansion variable ρ which is zero on the given flux surface, in terms of which the cylindrical

coordinates become

$$R(\rho, l) = R_s(l) + \rho \sin u, \quad (2.10a)$$

$$Z(\rho, l) = Z_s(l) + \rho \cos u. \quad (2.10b)$$

The metric tensor in these coordinates has non-zero components only on the diagonal (which is to be expected as we ensured orthogonality in the construction),

$$g_{ij} = \text{diag} \left[\left(1 - \frac{\rho}{R_c} \right)^2, 1, R^2 \right], \quad (2.11)$$

where we use the convention $x^1 = l$, $x^2 = \rho$, $x^3 = \phi$. The local solution is now constructed by expanding in ρ ,

$$\psi \approx \psi_0 + \rho \psi_1 + \frac{\rho^2}{2} \psi_2, \quad (2.12a)$$

$$p'(\psi) \approx p'(\psi_0) \quad (2.12b)$$

$$f'(\psi) \approx f'(\psi_0) \quad (2.12c)$$

and substitute into the Grad-Shafranov equation, which in leading order reduces to

$$\psi_2 = \left(\sin(u) + \frac{R_s}{R_c} \right) \frac{\psi_1}{R_s} - \mu_0 R_s^2 p'(\psi_0) - f(\psi_0) f'(\psi_0). \quad (2.13)$$

This allows one to find radial variation of the poloidal magnetic field by using (Helander & Sigmar 2005)

$$B_p = \frac{|\nabla \psi|}{R}, \quad (2.14)$$

resulting in

$$B_p(l, \rho) = \frac{\psi_1}{R_s} \left(1 + \rho \left[\frac{1}{R_c} - \frac{\mu_0 R_s^2 p'(\psi_0)}{\psi_1} - \frac{f(\psi_0) f'(\psi_0)}{\psi_1} \right] \right). \quad (2.15)$$

From this equation we can immediately see that $\psi_1/R_s = B_{p,s}$, with $B_{p,s}$ being the poloidal field on the flux-surface as indicated by the subscript. As such, the poloidal field strength can be written as

$$|B_p(l, \rho)| = B_{p,s} \left(1 + \rho \left[\frac{1}{R_c} - \frac{\mu_0 R_s p'}{B_{p,s}} - \frac{f f'}{R_s B_{p,s}} \right] \right) \equiv B_{p,s} (1 + \rho \partial_\rho b_p) \quad (2.16)$$

The toroidal field is found from its definition $B_\phi = f(\psi)/R$, resulting in

$$|B_\phi(l, \rho)| = B_{\phi,s} \left(1 + \rho \left[\frac{f'(\psi_0)}{f(\psi_0)} R_s B_{p,s} - \frac{\sin u}{R_s} \right] \right) \equiv B_{\phi,s} (1 + \rho \partial_\rho b_\phi), \quad (2.17)$$

where $B_{\phi,s} = f(\psi_0)/R_s$. The total magnetic field strength is also readily derived

$$B = \sqrt{B_{\phi,s}^2 + B_{p,s}^2} \left(1 + \rho \frac{B_{\phi,s}^2 \partial_\rho b_\phi + B_{p,s}^2 \partial_\rho b_p}{B_{\phi,s}^2 + B_{p,s}^2} \right) \equiv B_s (1 + \rho \partial_\rho b). \quad (2.18)$$

The radial variation of the poloidal line element is readily found from the metric tensor,

$$dl = \left(1 - \frac{\rho}{R_c} \right) [dl]_{\rho=0} \quad (2.19)$$

In these equations $f'(\psi_0)$ is treated as a free parameter, but it is difficult to ascertain if the chosen value of this parameter is realistic. It is more convenient, however, to specify

the magnetic shear, which is related to $f'(\psi_0)$. This can be made explicit by investigating the safety factor

$$q = \frac{f(\psi)}{2\pi} \int \frac{dl}{R_s^2 B_{p,s}}. \quad (2.20)$$

Taking the derivative of the safety factor with respect to ψ , one finds an equation describing this relationship,

$$\partial_\psi q = \frac{f'}{f} q + f \frac{1}{2\pi} \int \frac{dl}{R_s^3 B_{p,s}^2} \left(-\frac{2}{R_c} - \frac{2 \sin u}{R_s} + \frac{\mu_0 R_s p'}{B_{p,s}} + \frac{ff'}{R_s B_{p,s}} \right). \quad (2.21)$$

We also wish to relate the arclength along a magnetic field line to the poloidal arclength. These quantities are related as

$$dl = \left| \frac{B}{B_p} \right| dl. \quad (2.22)$$

Finally, the poloidal coordinate can be expressed in terms of the poloidal angle θ instead of the poloidal arclength by

$$l_\theta \equiv \frac{dl}{d\theta} = \sqrt{(\partial_\theta R_s)^2 + (\partial_\theta Z_s)^2}, \quad (2.23)$$

and the total arclength thus becomes

$$L = \oint l_\theta \left| \frac{B}{B_p} \right| d\theta. \quad (2.24)$$

2.3. Non-dimensionlisation and available energy

We proceed to make the various functions dimensionless as in Roach *et al.* (1995), and in doing so we will introduce various dimensionless constants which will be useful for the remainder of the analysis. We assume that we have been given the dependencies of the various functions in terms of the minor radial coordinate r , which in turn relates to the major radial coordinate R_0 via the inverse aspect ratio of the flux surface in question $\epsilon = r/R_0$. With these coordinates, we define various dimensionless functions,

$$\hat{R}_s = R/R_0, \quad (2.25a)$$

$$\hat{Z}_s = Z/R_0, \quad (2.25b)$$

$$\hat{R}_c = R_c/r, \quad (2.25c)$$

$$\hat{l}_\theta = l_\theta/r, \quad (2.25d)$$

$$\hat{B}_\phi = B_\phi/B_0, \quad (2.25e)$$

$$\hat{B} = B/B_0. \quad (2.25f)$$

One also needs to relate ψ to r , which can be done by investigating the poloidal field as in Eq. (2.14)

$$B_p = \frac{\partial_r \psi}{R_0} \frac{|\nabla r|}{\hat{R}_s}, \quad (2.26)$$

where we have made use of the relation $f(\psi_0) = B_0 R_0$. We go on to identify two factors in the above expression, namely

$$\partial_r \psi / R_0 \equiv B_{p,0} \quad (2.27)$$

and

$$\hat{B}_{p,s} \equiv |\nabla r| / \hat{R}_s. \quad (2.28)$$

Inserting these into the equation for the safety factor (2.20), one finds

$$B_{p,0} = \frac{\gamma\epsilon}{q} B_0, \quad \gamma \equiv \frac{1}{2\pi} \oint \frac{\hat{l}_\theta}{\hat{R}_s^2 \hat{B}_{p,s}} d\theta. \quad (2.29)$$

We proceed to define a dimensionless pressure gradient, analogous to the α parameter used in $s\text{-}\alpha$ geometry,

$$\alpha = -\frac{2\mu_0\epsilon^2 R_0^2 p'}{B_{p,0}} = -\epsilon r \frac{dp}{dr} \left/ \frac{B_{p,0}^2}{2\mu_0} \right. \quad (2.30)$$

Note that this dimensionless pressure gradient is unrelated to the Clebsch angle. The pressure gradient can in turn be used to define a dimensionless toroidal current density

$$\sigma = \left(\mu_0 p' + \frac{ff'}{R_0^2} \right) \frac{\epsilon R_0^2}{B_{p,0}} = \frac{q}{\gamma} f' R_0 - \frac{\alpha}{2\epsilon}. \quad (2.31)$$

We go on to define the shear s in the following manner

$$s = \epsilon R_0^2 B_{p,0} \partial_\psi \ln q = \frac{r}{q} \frac{\partial q}{\partial r} \quad (2.32)$$

which can be substituted into Eq. (2.21) to relate the shear to $f' R_0$ as

$$s = \frac{\gamma\epsilon^2}{q} f' R_0 - \frac{2}{\gamma} C_1 - \frac{2\epsilon}{\gamma} C_2 - \frac{\alpha}{2\gamma\epsilon} C_3 + \frac{q}{\gamma^2} C_4 f' R_0, \quad (2.33)$$

where we have defined the geometric constants C_1 to C_4 as

$$C_1 = \frac{1}{2\pi} \oint \frac{\hat{l}_\theta}{\hat{R}_c \hat{R}_s^3 \hat{B}_{p,s}^2} d\theta, \quad (2.34a)$$

$$C_2 = \frac{1}{2\pi} \oint \frac{\hat{l}_\theta \sin u}{\hat{R}_s^4 \hat{B}_{p,s}^2} d\theta, \quad (2.34b)$$

$$C_3 = \frac{1}{2\pi} \oint \frac{\hat{l}_\theta}{\hat{R}_s^2 \hat{B}_{p,s}^3} d\theta, \quad (2.34c)$$

$$C_4 = \frac{1}{2\pi} \oint \frac{\hat{l}_\theta}{\hat{R}_s^4 \hat{B}_{p,s}^3} d\theta. \quad (2.34d)$$

The radial derivatives of the magnetic field become

$$r \partial_\rho b_p = \left(\frac{1}{\hat{R}_c} - \frac{\alpha}{2\epsilon \hat{B}_{p,s}} \left[\frac{1}{\hat{R}_s} - \hat{R}_s \right] - \frac{\sigma}{\hat{R}_s \hat{B}_{p,s}} \right), \quad (2.35a)$$

$$r \partial_\rho b_\phi = \epsilon \left(\frac{\gamma^2 \epsilon}{q^2} \left[\sigma + \frac{\alpha}{2\epsilon} \right] \hat{R}_s \hat{B}_{p,s} - \frac{\sin u}{\hat{R}_s} \right). \quad (2.35b)$$

Finally, we express the total magnetic field length as

$$L = \frac{q\xi}{\gamma} R_0, \quad \xi \equiv \oint \frac{\hat{l}_\theta \hat{B}_s}{\hat{B}_{p,s}} d\theta. \quad (2.36)$$

We now turn our attention to the precession frequency, which we calculate from (1.3a). To simplify the calculation slightly, we note that the operator $\Delta\psi_t \partial_{\psi_t} \approx \Delta\psi \partial_\psi$ to leading order, as we can approximate $\Delta\psi_t \approx \Delta\psi \partial_\psi \psi_t$. Using this identity, we find the same

expression as in Roach *et al.* (1995),

$$\hat{\omega}_\alpha(\lambda) = \frac{\Delta\psi}{R_0^2 B_{p,0}} \left\langle \frac{1}{\epsilon} \left(2 \left[1 - \lambda \hat{B} \right] \left[r \partial_\rho b - r \partial_\rho b_p - \frac{1}{\hat{R}_c} \right] - \lambda \hat{B} r \partial_\rho b \right) \right\rangle_{\lambda} \quad (2.37)$$

where we define the bounce averaging operator in angular brackets as

$$\langle h \rangle_\lambda = \frac{\int d\theta h \cdot \hat{l}_\theta \frac{\hat{B}_s}{\hat{B}_{p,s}} / \sqrt{1 - \lambda \hat{B}}}{\int d\theta \hat{l}_\theta \frac{\hat{B}_s}{\hat{B}_{p,s}} / \sqrt{1 - \lambda \hat{B}}}. \quad (2.38)$$

We rewrite the precession frequency as

$$\hat{\omega}_\alpha \equiv \frac{\Delta\psi}{R_0^2 B_{p,0}} \hat{\omega}_\lambda. \quad (2.39)$$

Let us next investigate the Jacobian $\hat{g}^{1/2}$. We rescale it with a factor $\epsilon^{1/2}$, defining

$$\hat{g}_\epsilon^{1/2} \equiv \hat{g}^{1/2} \sqrt{\epsilon}. \quad (2.40)$$

The \mathbb{A} now becomes

$$A = \frac{3}{16} \frac{\Delta\psi_t \Delta\alpha L}{B_0} n_0 T_0 \sqrt{\epsilon} \left(\frac{\Delta\psi}{R_0^2 B_{p,0}} \right)^2 \frac{1}{\epsilon} \int_{\{\lambda\}} d\lambda \sum_{\text{wells}(\lambda)} I_z(c_0, c_1) \hat{\omega}_\lambda^2 \hat{g}_\epsilon^{1/2}, \quad (2.41)$$

where the prefactor $1/\epsilon$ to the integral deliberately not cancelled against the $\sqrt{\epsilon}$ to highlight that the integration range to lowest order $\{\lambda\} \sim \epsilon$, thus the integral is $\sim \mathcal{O}(\epsilon^0)$. With the above expression we go on to define a dimensionless \mathbb{A} . We take steps in line with (Mackenbach *et al.* 2022), and calculate the fraction of the total thermal energy that is available. The thermal energy of a plasma in a flux tube is to leading order in $\Delta\psi_t$,

$$E_t = \int \frac{3}{2} \frac{nT}{B} d\psi_t d\alpha d\ell = \frac{3}{2} n_0 T_0 \frac{\Delta\psi_t \Delta\alpha L}{B_0} \frac{1}{\xi} \oint \hat{l}_\theta \hat{B}_{p,s}^{-1} d\theta. \quad (2.42)$$

We then define the available energy as a fraction of the thermal energy as

$$\hat{A} = \frac{3A}{2E_t}. \quad (2.43)$$

Simplifying the expression using $\Delta\psi = \Delta r \partial_r \psi$, one finds that

$$\hat{A} = \frac{3}{16} \left(\frac{\Delta r}{R_0} \right)^2 \frac{\xi \sqrt{\epsilon}}{\oint \hat{l}_\theta \hat{B}_{p,s}^{-1} d\theta} \cdot \frac{1}{\epsilon} \int_{\{\lambda\}} d\lambda \sum_{\text{wells}(\lambda)} I_z(c_0, c_1) \hat{\omega}_\lambda^2 \hat{g}_\epsilon^{1/2}. \quad (2.44)$$

Δr measures the length-scale over which energy is available, i.e. a typical length-scale over which gradients can be flattened. We take this to be proportional to the correlation length, typically found to be the gyroradius. Hence we set

$$\Delta r = C_r \rho_g, \quad (2.45)$$

where ρ_g is the gyroradius, and C_r some function of order $\mathcal{O}(\rho_g^0)$. This function is not known *a priori*, and may vary. For example, if there are large radial streamers present in the system C_r may be significantly increased. However, for simplicity, we shall simply

take $C_r = 1$ below. The dimensionless \mathcal{A} now becomes

$$\hat{\mathcal{A}} = \frac{3}{16} \left(\frac{\rho_g}{R_0} \right)^2 \frac{\xi C_r^2 \sqrt{\epsilon}}{\oint \hat{l}_\theta \hat{B}_{p,s}^{-1} d\theta} \cdot \frac{1}{\epsilon} \int_{\{\lambda\}} d\lambda \sum_{\text{wells}(\lambda)} I_z(c_0, c_1) \hat{\omega}_\lambda^2 \hat{g}_\epsilon^{1/2}. \quad (2.46)$$

This expression has various scalings which are of interest. Firstly, we see that reducing the aspect ratio at fixed ρ_g/R_0 is beneficial since it leads to fewer trapped particles. Note that, in the limit of large aspect ratio, the trapping fraction scales as $\sqrt{\epsilon}$, which is the same dependency found here. A reduction in the expansion parameter ρ_g/R_0 (at fixed ϵ) is also found to help in decreasing \mathcal{A} .

As a final step, we introduce the dimensionless density gradient

$$R_0^2 B_{p,0} \partial_\psi \ln n = \frac{R_0}{n} \frac{\partial n}{\partial r} \equiv -\hat{\omega}_n, \quad (2.47)$$

with which c_0 and c_1 reduce to an especially simple form

$$c_0 = \frac{\hat{\omega}_n}{\hat{\omega}_\lambda} \left(1 - \frac{3}{2} \eta \right), \quad c_1 = 1 - \frac{\hat{\omega}_n}{\hat{\omega}_\lambda} \eta. \quad (2.48)$$

2.4. Miller geometry

Finally, we choose our equilibrium to be of the type discussed by Miller *et al.* (1998). The key step is to parameterise the flux surface as a standard D-shaped tokamak in terms of the poloidal angle θ ,

$$R_s(\theta) = R_0 + R_0 \epsilon \cos(\theta + \arcsin[\delta] \sin \theta), \quad (2.49a)$$

$$Z_s(\theta) = R_0 \kappa \epsilon \sin \theta. \quad (2.49b)$$

Here, $R_0(r)$ is the centre of the flux surface, $\kappa(r)$ is the elongation, and $\delta(r)$ is the triangularity. An important feature of this parameterisation is that it is up-down symmetric, which can be seen by invariance under $(Z_s, \theta) \mapsto -(Z_s, \theta)$. The poloidal magnetic field can then be calculated via (2.26), and the equilibrium is fully specified by the following set of 9 parameters; $[\epsilon, \kappa, \delta, s_\kappa, s_\delta, \partial_r R_0, q, s, \alpha]$, where $s_\kappa = r \partial_r \ln \kappa$ and $s_\delta = r \partial_r \arcsin(\delta)$. Henceforth we shall refer to this set of numbers which determines the local geometry as a “Miller vector”,

$$\mathbf{M} = [\epsilon, \kappa, \delta, s_\kappa, s_\delta, \partial_r R_0, q, s, \alpha]. \quad (2.50)$$

We finally plot a selection of cross-sections in Fig. 2, to serve as a reference for the various shapes mentioned in subsequent sections.

2.5. An analytical limit: large aspect ratio $s\text{-}\alpha$ tokamak

We proceed to investigate a limiting case of Miller geometries; namely that of a large aspect ratio tokamak with circular flux surfaces and a steep local pressure gradient. To this end, we set $\epsilon \ll 1$, $\kappa = 1$, and $\delta = s_\delta = s_\kappa = \partial_r R_0 = 0$, equivalent to the $s\text{-}\alpha$ tokamak investigated by Connor *et al.* (1983). In this limit we find that $\gamma = C_1 = C_3 = C_4 = 1$ and $C_2 = 0$, so that the equation for the shear simplifies to $s = \sigma - 2$. Furthermore, the prefactor $\xi / \oint \hat{l}_\theta \hat{B}_{p,s}^{-1} d\theta = 1$, and the same holds for $\hat{R}_s = \hat{B}_{p,s} = 1$ to lowest order in ϵ . The toroidal field becomes to first order in ϵ ,

$$B_\phi = B_0 \left(1 + \frac{\rho}{r} \epsilon \left[\frac{\alpha}{2q^2} - \cos \theta \right] \right), \quad (2.51)$$

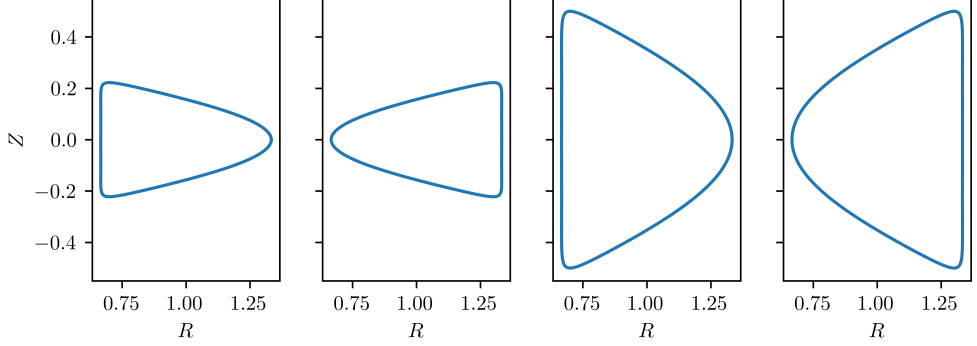


Figure 2: Cross sections in the (R, Z) -plane of tokamaks parameterized via Eq. (2.49). The parameters (κ, δ) are varied from the left-most to right-most plot as $(2/3, 0.9)$, $(2/3, -0.9)$, $(3/2, 0.9)$, and $(3/2, -0.9)$. All plots have $R_0 = 1$ and $\epsilon = 1/3$.

where the minus sign of the $\cos \theta$ term arises because θ and u have different directions. The poloidal field becomes

$$B_p = \frac{\epsilon B_0}{q} \left(1 + \frac{\rho}{r} [\alpha \cos \theta - s - 1] \right). \quad (2.52)$$

We use these expression to find the normalized drift ω_λ , to leading order in ϵ . To do so, we introduce a trapping parameter $k \in [0, 1]$, which relates to the pitch-angle like parameter λ as

$$\lambda = 1 + \epsilon(1 - 2k^2) \quad (2.53)$$

so that terms of the form $\lambda \hat{B}$ become to first order in ϵ

$$\lambda \hat{B} = 1 + \epsilon(1 - 2k^2 - \cos \theta). \quad (2.54)$$

With this, the drift precession frequency finally becomes

$$\hat{\omega}_\lambda = 2 \left\langle (2k^2 + \cos \theta - 1)(s - \alpha \cos \theta) - \left(\frac{\alpha}{4q^2} - \frac{\cos \theta}{2} \right) \right\rangle_\lambda. \quad (2.55)$$

The integrals that are to be evaluated are of two forms,

$$I_1 = \int (a + b \cos \theta) \sqrt{2k^2 + \cos \theta - 1} \, d\theta \quad (2.56)$$

and

$$I_2 = \int \frac{a + b \cos \theta}{\sqrt{2k^2 + \cos \theta - 1}} \, d\theta. \quad (2.57)$$

One can relate these various integrals to elliptical integrals of the first and second kind, which we define to be

$$K(k) \equiv \int_0^{\pi/2} \frac{d\zeta}{\sqrt{1 - k^2 \sin^2 \zeta}}, \quad (2.58a)$$

$$E(k) \equiv \int_0^{\pi/2} \sqrt{1 - k^2 \sin^2 \zeta} \, d\zeta. \quad (2.58b)$$

The first integral then becomes

$$\frac{I_1}{2\sqrt{2}} = 2 \left(a + \frac{b}{3} [2k^2 - 1] \right) E(k) + 2 \left(a + \frac{b}{3} \right) (k^2 - 1) K(k), \quad (2.59)$$

and the second integral becomes

$$\frac{I_2}{2\sqrt{2}} = 2bE(k) + (a - b)K(k). \quad (2.60)$$

Evaluating the precession frequency is now trivial, and we find that the result is the same as that of Connor *et al.* (1983),

$$\frac{\hat{\omega}_\lambda}{2} = \frac{E(k)}{K(k)} - \frac{1}{2} - \frac{\alpha}{4q^2} + 2s \left[\frac{E(k)}{K(k)} + k^2 - 1 \right] - \frac{2\alpha}{3} \left[\frac{E(k)}{K(k)} (2k^2 - 1) + 1 - k^2 \right]. \quad (2.61)$$

Furthermore, the Jacobian becomes

$$\hat{g}_\epsilon^{1/2}(k) = \frac{2\sqrt{2}}{\pi} K(k). \quad (2.62)$$

With all these expressions the \mathcal{AE} becomes a straightforward integral of known functions over k

$$\hat{A} = \frac{3}{2\pi\sqrt{2}} \left(\frac{\rho_g}{R_0} \right)^2 C_r^2 \sqrt{\epsilon} \int_0^1 dk k I_z(c_0, c_1) \hat{\omega}_\lambda(k)^2 K(k), \quad (2.63)$$

which can efficiently be computed numerically.

3. Numerical results

Two codes have been constructed: one that computes the integral of (2.63) using standard integration routines, and a first-order numerical routine that computes both the precession frequencies and the \mathcal{AE} as given in (2.43), both of which are computationally cheap (fractions of a CPU second per evaluation). We first investigate the results obtained for the s - α circular tokamak, after which we investigate how \mathcal{AE} varies in Miller geometries as a function of various parameters. The code used for generating these results is freely available on GitHub†. The bounce-integrals required in Eq. (2.43) are evaluated using numerical methods detailed in Mackenbach *et al.* (2023a). Finally we take the prefactor ρ_g/R_0 to be unity in all plots presented below, so when converting to a real device one should multiply the \mathcal{AE} by a factor $(\rho_g/R_0)^2$.

3.1. s - α geometry

A plot of the \mathcal{AE} calculated from Eq. (2.63) is given in Fig. 3 as a function of the magnetic shear and pressure gradient. We note that the ranges for s and α are not meant to represent realistically attainable values here, instead we are more interested in the general structure of the \mathcal{AE} over the domain. There are multiple interesting features visible in the figure. Even in this simplest model, the \mathcal{AE} exhibits rich structure over the s - α plane. The \mathcal{AE} is large when s and α are comparable, $s \sim \alpha$, and it is otherwise much smaller, particularly when the absolute value of one of these quantities is large. This is in line with previous findings (Dagazian & Paris 1982; Connor *et al.* 1983; Kessel *et al.* 1994; Strait *et al.* 1997; Rettig *et al.* 1997; Kinsey *et al.* 2006). It is furthermore interesting to note that the precise reduction in \mathcal{AE} depends on the drive: for a pure

† Install the code via <https://github.com/RalfMackenbach/AE-Miller>

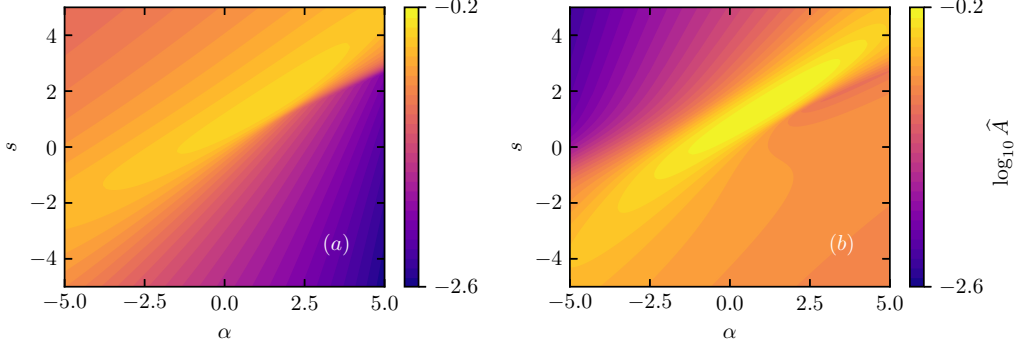


Figure 3: The \hat{A} of a large aspect ratio circular tokamak, as a function of magnetic shear s and pressure gradient α . The plots have been generated using $q = 2$. Plot (a) has $\hat{\omega}_n = 3$ and $\eta = 0$, whereas plot (b) has a pure electron temperature gradient, i.e. $\hat{\omega}_n = 0$ and $\hat{\omega}_n \eta = 3$.

electron-temperature gradient, significant positive shear is most helpful in reducing \hat{A} , whereas the \hat{A} driven by a pure density gradient benefits more from negative shear.

Since Eq. (2.63) can be integrated numerically to high precision, it serves as a useful benchmark for the more general \hat{A} of (2.43). Accordingly, we have compared the \hat{A} in the large-aspect-ratio limit with circular flux surfaces using a code which solves Eq. (2.43). This comparison is shown in Appendix A, and we find that the codes agree.

3.2. Miller geometry

We now leave the realm of the $s\text{-}\alpha$ limit and venture into shaped, finite-aspect-ratio equilibria. Our first step is to investigate the dependence on magnetic shear and pressure gradient for a range of different Miller vectors, and the results are shown in Fig. 4. Here we see similar trends as in section 3.1: negative shear and large α tend to be especially stabilising for a pure density gradient. It is however also clear that the magnitude and precise contours depend *strongly* on the chosen Miller vector, as defined in Eq. (2.50). For example, it can be seen that lowering the safety factor is very stabilising, as the \hat{A} is reduced over a large region of the $s\text{-}\alpha$ plane as one compares subfigure (a) to (b). In subfigure (c) the elongation has been reduced produce a ‘‘comet’’-type configuration ($\kappa < 1$, i.e. a horizontally elongated tokamak, see Fig. 2), which can decrease the magnitude of the \hat{A} , though the stabilising effects of s and α become less pronounced. Finally, in subfigure (d) the sign of the triangularity has been reversed to become negative. Though the shape of the contours is largely unchanged, the peak in \hat{A} is shifted to higher α and lower s , indicating that negative triangularity can be particularly beneficial in high-shear discharges with a modest value for α . In a more general sense, when changing any of the parameters significantly one should expect that the precise shape and magnitude of the contours changes non-trivially.

With this important caveat in mind, let us investigate the influence of geometry on the \hat{A} . To do so, we display the dependence on κ and δ for various Miller vectors in Fig. 5. Several general interesting trends can be noted. Firstly, we see that it is not true *in general* that either positive or negative triangularity is always stabilising; it depends on the other Miller parameters. Secondly, we see that tokamaks with $\kappa < 1$ and $\delta < 0$, often referred to as (negative) comet-cross-sections tokamaks (Kesner *et al.* 1995), are possible contenders for \hat{A} -minimizing geometries. This is perhaps unsurprising, as such tokamaks are close to having the maximum- \mathcal{J} property as shown by Miller *et al.* (1989).

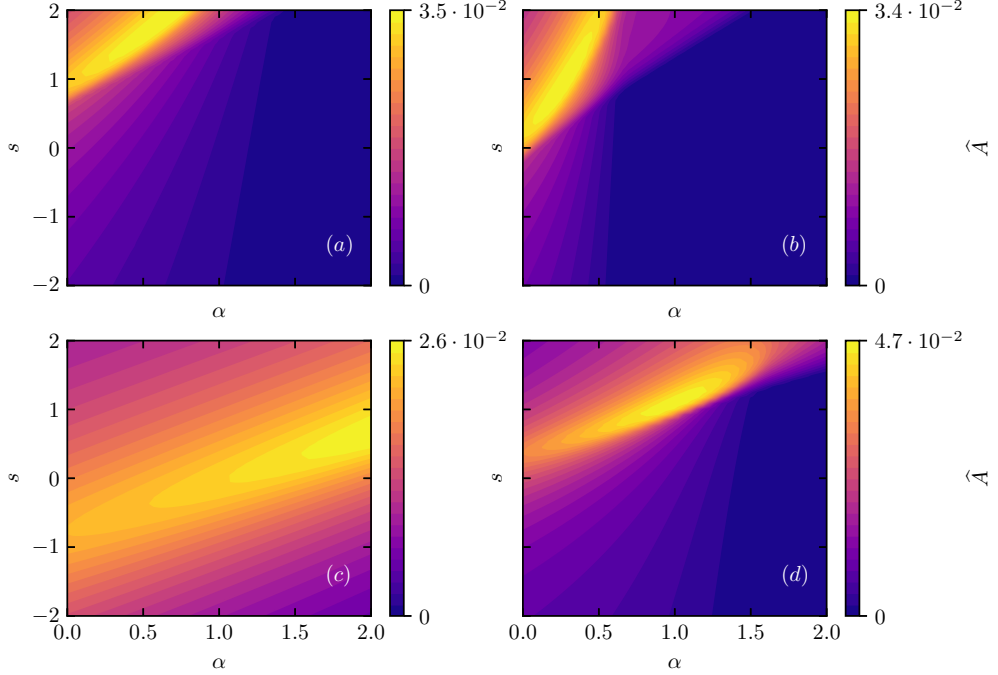


Figure 4: Dependence of \bar{A} on magnetic shear s and pressure gradient α . In subplot (a), the Miller vector $[\epsilon, \kappa, \delta, s_\kappa, s_\delta, \partial_r R_0, q, s, \alpha]$ is set to $[1/3, 3/2, 1/2, 0, 0, 0, 2, s, \alpha]$, and other plots have the same vector with one parameter changed. In subplot (b) the safety factor q is lowered from 2 to 1, for (c) the elongation κ is decreased from $3/2$ to $1/2$, and in (d) the sign of the triangularity δ is flipped from $1/2$ to $-1/2$. All plots have $\hat{\omega}_n = 1$ and $\eta = 0$.

Since \bar{A} measures deviations from the maximum- \mathcal{J} property, it is thus expected that these configurations perform well in terms of \bar{A} . Investigating the plots in detail, we first note that increasing the inverse aspect ratio, as is done when going from (a) to (b), has a stabilising effect. Naively, one would expect that doubling the aspect ratio would increase the \bar{A} by roughly a factor $\sqrt{2} \approx 1.4$, due to the factor $\sqrt{\epsilon}$ in Eq. (2.44). However, going from plot (a) to (b) we see an increase of the maximum by a factor ~ 1.1 , which is significantly less than $\sqrt{2}$. This is likely due to the fact that, in a small-aspect-ratio device, magnetic field lines spend most of their time (or more precisely, arc-length) on the inboard side of the tokamak (Helander & Sigmar 2005). There, ω_λ tends to be opposite to the drift wave and therefore these orbits do not contribute to the \bar{A} for a pure density gradient. Going from plot (a) to (c) the safety factor is halved, resulting in the contours changing shape significantly. It is furthermore interesting to note that the largest \bar{A} increases by some 25% when the safety factor drops, which indicates that there is significant interplay between shaping and the safety factor. Finally, plot (d) has significant positive shear as compared to (a), which drastically changes the picture. As in Fig. 4, we again find that significant positive shear leads to negative triangularity being preferable to positive triangularity. It is also interesting to note that with significant positive shear, the negative-comet tokamak is no longer an \bar{A} -minimizing geometry. We find that the results change somewhat if one instead imposes a pure electron temperature

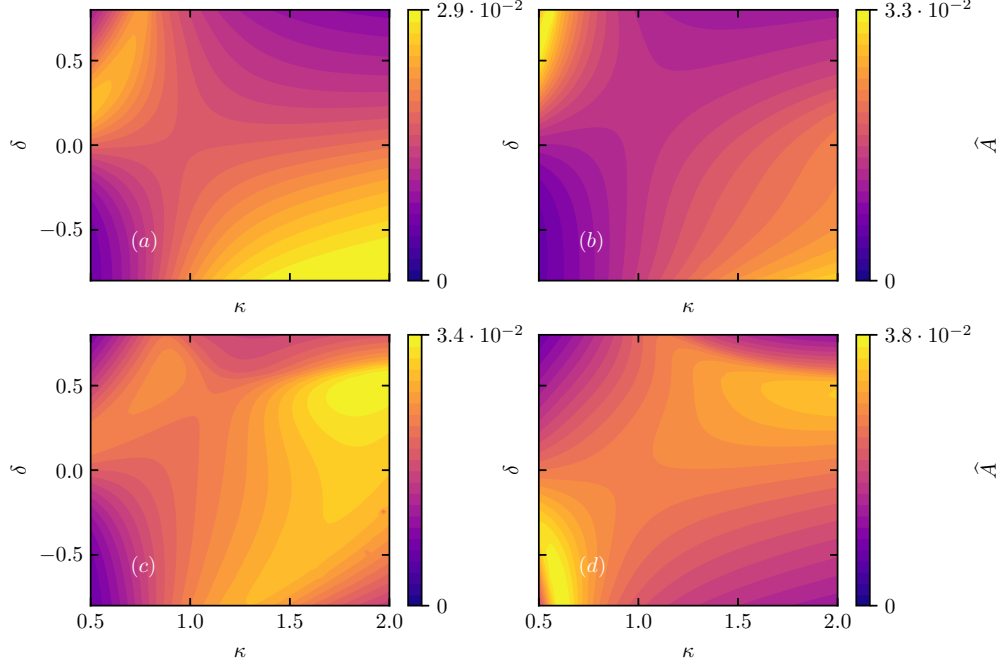


Figure 5: The effect of the geometry on $\bar{A}\mathcal{E}$. In plot (a) the Miller vector $[\epsilon, \kappa, \delta, s_\kappa, s_\delta, \partial_r R_0, q, s, \alpha]$ is set to $[1/3, \kappa, \delta, 0, 0, 0, 2, 0, 0]$, and all other subfigures have the same Miller vector with one parameter changed. The contours showcased in (b) has the inverse aspect ratio is raised from $1/3$ to $2/3$, in (c) the safety factor is decreased from 2 to 1 , and for (d) we have increased the shear from 0 to 2 . All plots have $\hat{\omega}_n = 1$ and $\eta = 0$.

gradient (not shown here), though the basic trends remain intact, apart from the large aspect-ratio stabilisation.

All in all, we conclude from these results that the $\bar{A}\mathcal{E}$ is very sensitive to equilibrium parameters, including quantities not investigated here such as s_κ , η , and $\partial_r R_0$. This sensitivity is perhaps reassuring: gyrokinetic turbulence has long been known to be strongly dependent on equilibrium parameters and even slight nudges can drastically change the picture (a sentiment perhaps best captured by the old Dutch expression *wie het kleine niet eert, is het grote niet weerd*). We seem to reproduce similar sensitivity in this simplified $\bar{A}\mathcal{E}$ -model for trapped electrons. This sensitivity becomes especially clear when investigating the dependence of $\bar{A}\mathcal{E}$ on triangularity, which we shall do in the next section.

3.3. When is negative triangularity beneficial?

As hinted at in the previous section, it is not possible to make a general statement about the effect of negative triangularity on $\bar{A}\mathcal{E}$; its possible benefit depends strongly on other parameters describing the equilibrium. We can however find trends, and in order to do so we define the following fraction

$$\Delta = \frac{\bar{A}(\delta = -0.1)}{\bar{A}(\delta = +0.1)}, \quad (3.1)$$

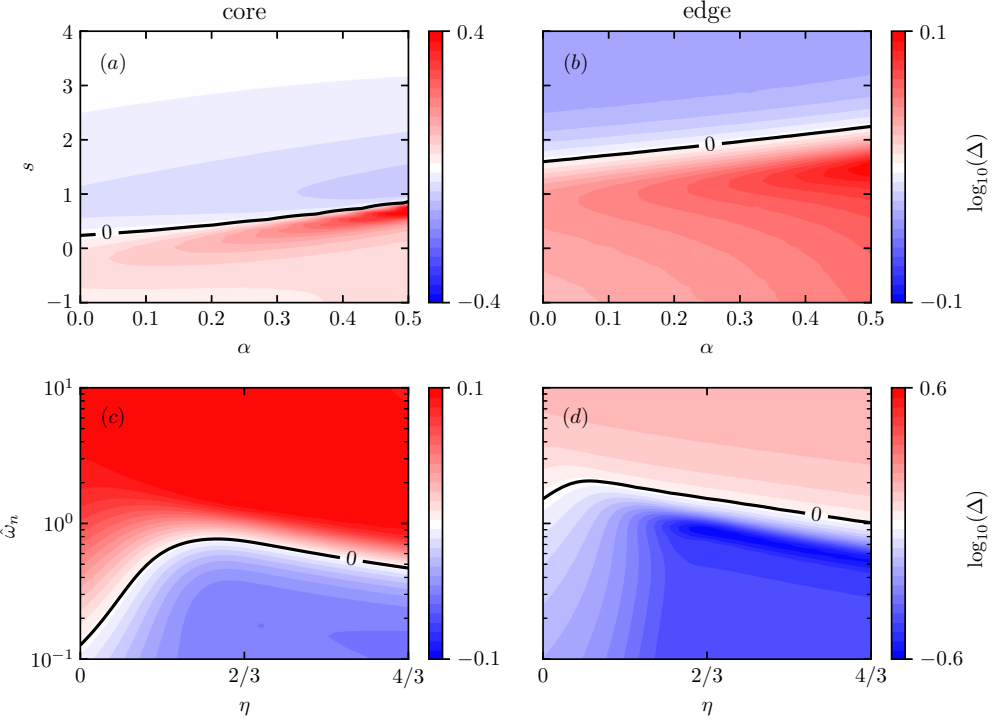


Figure 6: Various plots showcasing the dependencies of $\log(\Delta)$, where Δ is defined as $\widehat{A}(\delta = -0.1)/\widehat{A}(\delta = +0.1)$, on various equilibrium parameters. The two columns have different Miller vectors $[\epsilon, \kappa, \delta, s_\kappa, s_\delta, \partial_r R_0, q, s, \alpha]$, which are meant to be representative of the edge and the core. The first column has a core-like Miller vector of $\mathbf{M}_{\text{core}} = [1/100, 3/2, \delta, 0, 0, 0, 1, s, \alpha]$. The second column has an edge-like Miller vector of $\mathbf{M}_{\text{edge}} = [1/3, 3/2, \delta, 1/2, 0, -1/2, 3, s, \alpha]$. Finally, plot (a) has $\hat{\omega}_n = 1/2$ and $\eta = 0$, (b) has $\hat{\omega}_n = 2$ and $\eta = 0$, plot (c) has $s = \alpha = 0$, and (d) has $s = 2$ and $\alpha = 1/2$.

where $\delta = \pm 0.1$ is chosen to represent a typical experimentally realizable range of parameters. This fraction can be interpreted as the factor by which the \mathcal{A} changes upon switching from positive to negative triangularity, where $\Delta < 1$ implies a reduction in \mathcal{A} . We present an investigation of Δ and its dependencies in Fig. 6. We see two clear trends which seem to be robust for tokamaks with $\kappa > 1$. Firstly, as noted in the previous sections, in plots (a) and (b) we see that negative triangularity tends to be especially stabilising for configurations with significant positive shear. Similar conclusions were made by Merlo & Jenko (2023), who found that the turbulent heat-flux in gyrokinetic simulations follows the same trend for TEM-driven turbulence: only for sufficiently high positive shear is a decrease in heat flux found at negative triangularity. Increasing α tends to push the $\Delta = 1$ line (in the plot this is the $\log \Delta = 0$ line) to even higher values of shear, implying that a significant pressure gradient may make negative triangularity less desirable. Secondly, in plots (c) and (d) we note that negative triangularity can be beneficial in situations where the gradient is small, such as in the core. The dependence on η is non-trivial; at small density gradients a nonzero value of η can make negative triangularity beneficial. As in the previous sections, the results here depend on the Miller vector and are not meant to serve a quantitative measure for core and edge transport.

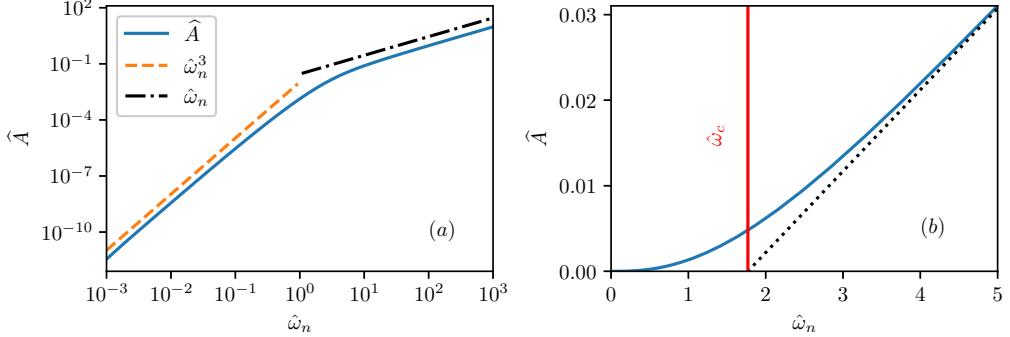


Figure 7: Example of dependence of \bar{A} on gradient strength. Two scalings are found in plot (a). In plot (b) we define a gradient threshold by fitting a straight line to the strongly driven regime, and finding its $\hat{\omega}_n$ interception with the abscissa.

We have, however, found that the presented trends tend to be robust as long as $\kappa > 1$ and thus do have *qualitative* value. We finally note that a more comprehensive model of the effect of negative triangularity should likely take collisions, impurities, and global effects into account (Merlo *et al.* 2019, 2021).

From these results we infer that negative triangularity is expected to be especially beneficial in the core of the plasma, where gradients are necessarily small. It is not clear if the benefit extends to the edge: only with significant positive shear does negative triangularity become beneficial here as well. One should also keep in mind that Δ measures the effect of going to negative triangularity whilst keeping all other parameters fixed. A more complete investigation would, for example, compare experimental equilibria with positive and negative triangularity, or use a global MHD-equilibrium code to find consistent profiles. We do not attempt such an investigation here, but we note that our mathematical framework would readily allow for such a comparison. We finally remark that the above results may seem counter-intuitive, as negative triangularity is often thought to automatically imply TEM stabilisation since the bounce points of most trapped particles reside on the inboard side of the torus, where the magnetic curvature should be favourable. Consequently, it is often argued that the bounce-averaged drift is such that TEMs are stabilised. Upon calculation of (2.37), we find no such stabilisation however, as explained further in Appendix B.

3.4. Gradient-threshold like behaviour

Our next step is to investigate the dependence of \bar{A} on the gradient strength $\hat{\omega}_n$. From Eq. (2.8), one can show that there are two distinct scalings (Mackenbach *et al.* 2023b). In a strongly driven regime one finds that the \bar{A} scales linearly with the gradient strength $\hat{\omega}_n$. For a weakly driven regime one can expand around small $\hat{\omega}_n$, and one finds that the \bar{A} scales with the gradient strength as $A \propto \hat{\omega}_n^3$,

$$\hat{A} \propto \begin{cases} \hat{\omega}_n & \text{if } |\hat{\omega}_n| \gg 1, \\ \hat{\omega}_n^3 & \text{if } |\hat{\omega}_n| \ll 1. \end{cases} \quad (3.2)$$

These scalings are reminiscent of gradient-threshold (or critical-gradient) type behaviour (Dimits *et al.* 2000). Gradient thresholds are signified by a sudden decrease in heat-flux when decreasing the gradient below some threshold value. The aforementioned scaling behaviour of the \bar{A} is displayed in Fig. 7 which similarly shows a rapid decrease below

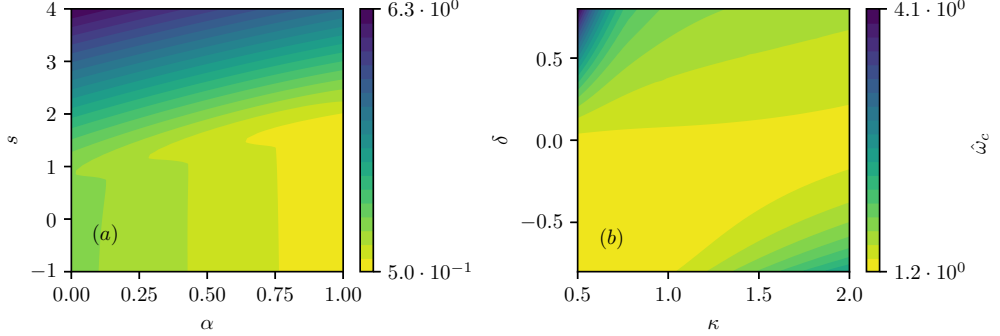


Figure 8: The gradient threshold as a function of equilibrium parameters. In plot (a) the Miller vector $[\epsilon, \kappa, \delta, s_\kappa, s_\delta, \partial_r R_0, q, s, \alpha]$ is $[1/3, 3/2, 1/2, 0, 0, 0, 2, s, \alpha]$, and plot (b) has $[1/3, \kappa, \delta, 0, 0, 0, 0, 2, 0, 0]$. In all plots $\eta = 0$.

some threshold value. In plot (b) we estimate a critical-threshold like quantity from \mathcal{A} , by fitting a straight line to the strongly driven regime, i.e. we find the best-fit parameters a_0 and a_1 in the formula

$$\hat{A} = a_0 + a_1 \hat{\omega}_n, \quad (3.3)$$

with $\hat{\omega}_n \gg 1$. The gradient threshold, denoted by $\hat{\omega}_c$, is then defined as the interception with the abscissa, hence

$$\hat{\omega}_c \equiv -\frac{a_0}{a_1}. \quad (3.4)$$

One could, of course, use different definitions for $\hat{\omega}_c$, e.g. one could define the intersection point between the two straight lines on the log-log plot of Fig. 7 as $\hat{\omega}_c$. We have however found that the definition of Eq. (3.4) has several benefits: it is computationally cheaper, less prone to numerical noise, and seems to behave more smoothly. Other attempted definitions do show the same trends.

We illustrate how $\hat{\omega}_c$ varies as a function of various equilibrium parameters in Fig. 8. Note that subplot (a) in Fig. 8 has the same Miller vector as Fig. 4 (a), and subplot (b) in Fig. 8 has the same Miller vector as Fig. 5 (a). One interesting trend is that increasing the shear tends to increase $\hat{\omega}_c$ linearly, and $\hat{\omega}_c$ tends to plateau for low shear to some value. This is similar to findings of Jenko *et al.* (2001), though their investigation focusses on electron-temperature-gradient turbulence. It is also interesting to note that, although the \mathcal{A} is high in the negative-triangularity configuration, it does benefit from a high critical gradient, which is in line with findings of Merlo *et al.* (2015). This effect becomes even more pronounced as one increases the shear, which furthermore reduces the \mathcal{A} in the negative triangularity configuration. This implies that negative triangularity may be beneficial in a different sense: since the critical gradient as estimated from \mathcal{A} is higher in negative triangularity discharges the profiles are able to sustain much higher gradients and thus higher core density/temperature.

3.5. Tokamak optimisation

In this section we aim to find \mathcal{A} -optimised tokamaks for a certain set of equilibrium parameters, at fixed gradients ($\hat{\omega}_n = 1$ and $\eta=0$). To this end, we choose to optimise over κ and δ whilst keeping all other parameters fixed. In order to find somewhat realistic

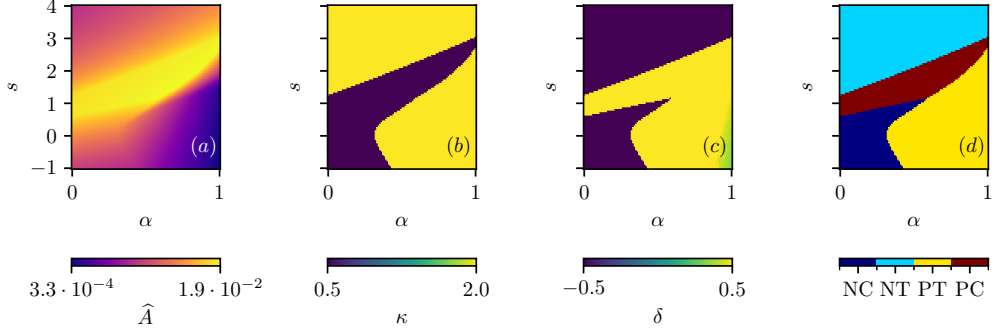


Figure 9: Global $\mathcal{A}\mathcal{E}$ -minimizing solutions as a function of s and α . Plot (a) showcases the $\mathcal{A}\mathcal{E}$ of the optimal solution, (b) displays the elongation, (c) shows the triangularity, and (d) presents the type of reactor geometry. Generated with a Miller vector $[\epsilon, \kappa, \delta, s_\kappa, s_\delta, \partial_r R_0, q, s, \alpha]$ of $[1/3, \kappa, \delta, 0, 0, -1/2, 3, s, \alpha]$. In all plots $\hat{\omega}_n = 1$ and $\eta = 0$.

solutions, we restrict ourselves to a bounded optimisation space, namely

$$\kappa \in (1/2, 2), \quad \delta \in (-1/2, 1/2). \quad (3.5)$$

The SHGO algorithm from Endres *et al.* (2018) is ideally suited for finding the global minimum in this low-dimensional bounded parameter-space, and is furthermore available in `scipy`. Finally, we shall vary magnetic shear and α , and investigate its effect on the found global minimum.

The results are displayed in Fig. 9, where the minimal $\mathcal{A}\mathcal{E}$, κ , and δ values are displayed as a function of s and α . We furthermore succinctly display the type of geometry in plot (d) by distinguishing between four different geometries; we refer to $\kappa < 1$ and $\delta < 0$ as negative comet (NC), $\kappa > 1$ and $\delta < 0$ as negative triangularity (NT), $\kappa > 1$ and $\delta > 0$ as positive triangularity (PT), and finally $\kappa < 1$ and $\delta > 0$ as positive comet (PC). Similar cross-sections may be seen in Fig. 2. It can be seen that both the optimal triangularity and elongation tend to be in the corners of the optimisation domain, and hence one should expect that these results are strongly dependent on this domain. It is interesting to note that the NT solution tends to be optimimal whenever there is significant shear and the pressure gradient is not too large, which is in line with the findings of section 3.3.

From this plot an important conclusion can be drawn: there is no such thing as a single ‘‘optimal’’ solution. The global minimum depends sensitively on other equilibrium parameters such as shear and pressure gradient, which are in turn determined by the profiles of the safety factor, density, and temperature. Hence, if one were interested in finding an $\mathcal{A}\mathcal{E}$ -optimised tokamak one should take care in choosing the right profiles. One could also choose to let the profiles be part of the optimisation, by describing them with some number of free parameters and constraints (e.g. one could use a fixed number Fourier modes on top of a profile and optimise for the mode amplitudes). In reality, the profiles are themselves set by equilibrium conditions, making a self-consistent optimisation highly non-trivial. A more consistent investigation could perhaps solve this by coupling the current $\mathcal{A}\mathcal{E}$ -model to a transport solver, which would calculate self-consistent profiles.

3.6. Existence of solutions with high gradients yet low \mathcal{A}

In this section, we investigate how this \mathcal{A} model may relate to the suppression of TEMs when the density gradient is increased. To do so, we note several interesting properties that arise as one increases this gradient. Firstly, the normalized pressure gradient α scales linearly with the density gradient (assuming a constant ratio of poloidal magnetic field pressure to thermal pressure). The shear depends on the pressure gradient, as such a gradient drives the bootstrap current, which in turn changes the rotational transform profile. The bootstrap current density has an off-axis maximum in realistic scenarios, and such an off-axis maximum can locally lower the shear. This is most readily seen by inspecting the expression for shear in a large-aspect-ratio, circular tokamak, which depends on the current density profile $j(r)$ as

$$s(r) = 2 \left(1 - \frac{j(r)}{\bar{j}(r)} \right); \quad \bar{j}(r) = \frac{2}{r^2} \int_0^r x j(x) dx, \quad (3.6)$$

where \bar{j} measures the average current density inside the radius r . From this expression, it is clear that for current-density profiles which peak at $r = 0$, the shear is always positive. An off-axis maximum, supplied by the bootstrap current, can cause a locally lower shear. Hence, as one raises $\hat{\omega}_n$ one simultaneously increases α and decreases s . To estimate the magnitude of the effect of the bootstrap current on the shear, we note that the bootstrap current is proportional to the density and temperature gradients, and thus to the pressure gradient

$$j_b \approx j_{b,0} \alpha(r). \quad (3.7)$$

This is an approximation since the different transport coefficients relating the bootstrap current to the various gradients are not identical (Helander & Sigmar 2005), but we ignore this minor complication. We furthermore write the total current density as $j = j_b + j_e$, where j_e is the equilibrium current, and assume $j_b \ll j_e = j_{e,0} \hat{j}(r)$. To first order in the smallness of the bootstrap current, (3.6) then gives

$$s \approx 2 - \frac{r^2 \hat{j}(r)}{\int_0^r x \hat{j}(x) dx} \left(1 + \frac{j_{b,0}}{j_{e,0}} \left[\frac{\alpha(r)}{\hat{j}(r)} - \frac{\int_0^r x \alpha(x) dx}{\int_0^r x \hat{j}(x) dx} \right] \right). \quad (3.8)$$

Finally, following Miyamoto (2005) we estimate the ratio $j_{b,0}/j_{e,0}$ as

$$\frac{j_{b,0}}{j_{e,0}} \approx 0.3 \langle \beta_p \rangle \sqrt{\epsilon}, \quad (3.9)$$

where β_p is the local ratio of the thermal pressure over the poloidal magnetic field pressure, and the angular brackets denote a volume average. We shall take $j_{b,0}/j_{e,0}$ to be on the order of 10%, implying that the shear may change as $ds/d\alpha \sim s/10$. Finally, one can relate the pressure gradient to $\hat{\omega}_n$ as

$$\alpha = \epsilon \beta_p (1 + \eta + \eta_i) \hat{\omega}_n, \quad (3.10)$$

where $\eta_i = \partial_r \ln T_i / \partial_r \ln n$, with $T_i(r)$ being the ion temperature. We assume that the factor $\epsilon \beta_p (1 + \eta + \eta_i) \sim 0.1$, so that $d\hat{\omega}_n/d\alpha \sim 10$.

We illustrate the competing effects of the density gradient, pressure gradient, and shear in Fig. 10. In subfigures (a) and (b) we see various iso-contours of the \mathcal{A} in $(\hat{\omega}_n, s, \alpha)$ -space, where (a) has positive triangularity and (b) has negative triangularity. It is especially interesting to note that in subfigure (a) there are paths in parameter space in which $\hat{\omega}_n$ increases but the \mathcal{A} decreases. These paths generally require that, as the density gradient increases, the pressure gradient should also increase and the shear should decrease. As

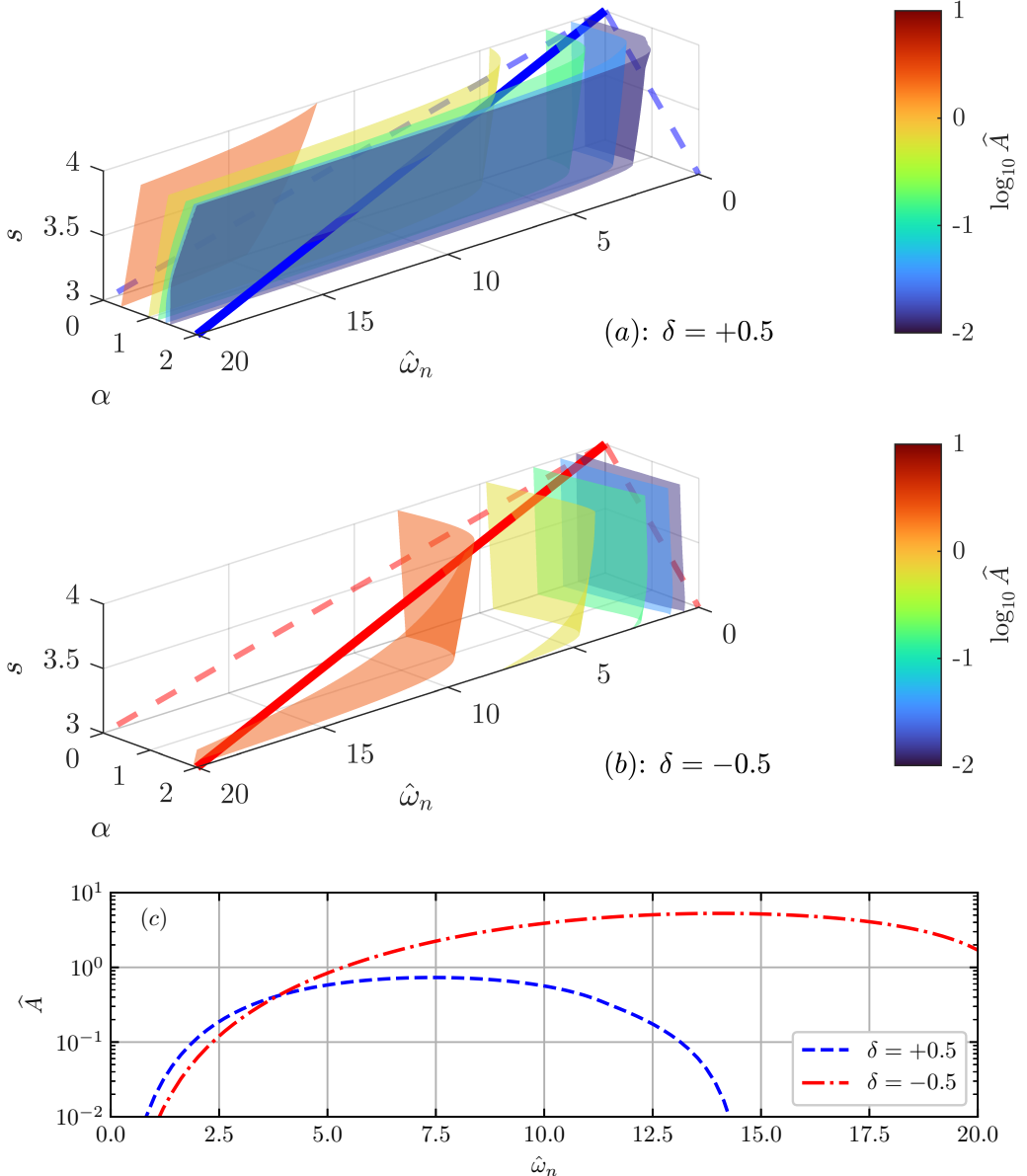


Figure 10: subfigures (a) and (b) showcase iso-contours of the \hat{A} as a function of $(\hat{\omega}_n, \alpha, s)$, where subfigure (a) and (b) have positive and negative triangularity respectively. In both (a) and (b) a straight line is drawn which has increasing α and decreasing s with increasing $\hat{\omega}_n$, and the projection of the line onto the grid-planes is shown as a dashed line. In subfigure (c), the \hat{A} along both the blue line of subfigure (a) and the red line of subfigure (b) is plotted as a function $\hat{\omega}_n$. These plots were generated with a Miller vector $[\epsilon, \kappa, \delta, s_\kappa, s_\delta, \partial_r R_0, q, s, \alpha]$ of $[1/3, 3/2, \delta, 1/2, \delta/\sqrt{1-\delta^2}, -1/2, 3, s, \alpha]$, and $\eta = 0$.

we have argued, these trends are indeed found in tokamak discharges. One such path is indicated in subplot (a) as a blue line. Importantly, the blue line has

$$s = 4 \left(1 - \frac{\alpha}{8}\right), \quad \hat{\omega}_n = 10 \cdot \alpha$$

which is the right order of magnitude for both $ds/d\alpha$ and $d\hat{\omega}_n/d\alpha$. Subfigure (b) exhibits drastically different features. Planes of constant $\mathcal{A}E$ tend to lie parallel to planes of constant $\hat{\omega}_n$, indicating that not much stabilisation is possible by changing the shear or the pressure gradient: the $\mathcal{A}E$ rises when $\hat{\omega}_n$ is increased. In subfigure (b), we again plot a line along the direction of increasing α and decreasing magnetic shear in red. Finally, note that for s_δ we have used the estimate from Miller *et al.* (1998), $s_\delta \approx \delta/\sqrt{1-\delta^2}$.

In subfigure (c) we display the $\mathcal{A}E$ along the blue and red lines given in subfigures (a) and (b) as a function of the density gradient. Note that the positive-triangularity case exhibits a distinct maximum, with low $\mathcal{A}E$ both to the left and right of the peak. One could interpret the existence of the latter as two distinct low-transport regimes; one with low gradients, and one with high gradients (which also has decreased magnetic shear and increased α). It is furthermore interesting to note that the negative-triangularity tokamak rises to far higher values in terms of $\mathcal{A}E$ and does not seem to drop back down to low levels along the chosen domain. Hence one could perhaps conclude that reaching a low-transport state with high gradients is not feasible in a negative-triangularity discharge. This is in line with findings of Saarelma *et al.* (2021) and Nelson *et al.* (2022), where the H-mode was found to be inaccessible in negative-triangularity tokamaks on basis of the ballooning instability, though the physical reason is of course different. This rise in $\mathcal{A}E$ in negative triangularity is perhaps unsurprising given that we have found that negative triangularity is stabilising in cases with significant positive shear, a weak pressure gradient, and a slight density gradient, exemplified in Figs. 6 and 9. Since, along the chosen path shear decreases and α increases with increasing density gradient, which is opposite to what is stabilising for negative-triangularity tokamaks, we see a sharp increase in $\mathcal{A}E$. It may be feasible, however, to have a significant reduction in transport by tailoring the q -profile in such a way that negative triangularity becomes favorable, which likely implies significant positive shear. With such a reduction in $\mathcal{A}E$, one could perhaps enjoy much improved transport whilst staying in an L-mode like regime. The parameters described in Marinoni *et al.* (2019) do seem to meet such requirements, especially near the edge where the reduction in transport seems greatest as compared to the positive triangularity case.

A more comprehensive investigation, which shall be undertaken in a future publication, would self-consistently calculate the bootstrap current which would give precise paths in $(\hat{\omega}_n, \alpha, s)$ -space. However, given the nature of the iso-contours in this three-dimensional space, we expect the observed trends to be robust, as long as the path has the correct general dependencies (i.e. decreasing shear and increasing α with increasing density gradient).

3.7. Comparison with TGLF

Finally, after investigating the dependence of the $\mathcal{A}E$ on various parameters we compare it with turbulent energy-flux calculations in tokamak geometry. At the moment, nonlinear gyrokinetic simulations are computationally too expensive for detailed two-dimensional scans like those shown in Fig. 4 and 5, therefore we instead employ the quasi-linear TGLF (trapped gyro-Landau fluid) code (Staebler *et al.* 2007; Staebler & Kinsey 2010). A few key differences between the two models are highlighted before any comparison is made. TGLF computes the linear eigenmodes of a variety of instabilities, ion and

electron temperature gradient (ITG, ETG) modes, electromagnetic kinetic ballooning (KB) modes, as well as trapped-ion and trapped-electron modes (TIM, TEM), and then applies a quasilinear saturation rule to accurately fit the fluxes from nonlinear gyrokinetic simulations. For quasi-neutrality purposes TGLF requires the inclusion of at least one ion species. These are fundamental differences to the formulation of the $\mathcal{A}E$ described in this work, which only accounts for the $\mathcal{A}E$ of trapped electrons. Therefore, when setting up TGLF, care was taken to ensure the modelled turbulent energy-fluxes were as much as possible due to instabilities dominated by trapped electrons, using settings analogous to those used in recent gyrokinetic simulations in a similar regime (Proll *et al.* 2022). Given the lack of collisions in this regime, the expected dominant instabilities should be of the collisionless trapped-electron mode (CTEM) variety. Nevertheless, some other instabilities can also arise due to interactions with the ion population, such as the ubiquitous mode Coppi & Pegoraro (1977). Thus, to ensure that the dominant instabilities in the TGLF simulations were as relevant as possible for our comparison, only contributions from modes propagating in the electron diamagnetic direction were included, as e.g. the ubiquitous mode is characterized by a change in mode propagation direction. Furthermore, we find that, for the scenarios considered in this work, adding an equally large electron temperature gradient to the density gradient, i.e. taking $\eta = 1$, significantly decreased the amount of non-TEM modes dominant in TGLF simulations, and as such we set η to unity for the comparison. The ETG mode can play a role (at large wavenumbers) under such conditions, which the current $\mathcal{A}E$ also does not model, but this effect is more benign. The recent SAT2 (Staebler *et al.* 2021) quasilinear saturation rule for TGLF was used, as it includes the proper impact of plasma shaping on the quasilinear saturation (Staebler *et al.* 2020). Although TGLF also uses a Miller parameterization of the local equilibrium, we note that it does not use the same normalization as Roach *et al.* (1995) followed in this work, and care has been taken in converting between the two.

There is an additional, more fundamental, difficulty one needs to account for in such a comparison. When supposing that the length-scale over which energy is available is proportional to the gyroradius in Eq. (2.45), we have not specified *which* gyroradius is meant. The gyroradius scales inversely proportional to some reference magnetic field B_{ref} , i.e.

$$\rho_g \propto \frac{1}{B_{\text{ref}}}. \quad (3.11)$$

Hence the choice of the reference magnetic field can impact the total $\mathcal{A}E$, and it is unclear *a priori* what an appropriate choice is. Let us denote a generically chosen reference field by $B_{\text{ref}} = C_B B_0$, where C_B is a dimensionless number which relates to the choice of B_{ref} . Formally, one could absorb any choice of C_B into C_r of Eq. (2.45). TGLF offers two options, $C_B = \gamma$ (as in Eq. (2.29)) and $C_B = 1$.[†] Encouragingly though, for realistic equilibria $C_B \approx \text{constant}$ for many choices of the reference field (e.g. $\gamma \approx 1$ for equilibria which are not strongly shaped). However, when venturing into the strongly shaped realm (e.g. $|\delta| > 0.3$ and $\kappa > 3/2$) the choice of B_{ref} can have a significant impact in both TGLF and $\mathcal{A}E$. Running TGLF with $C_B = \gamma$ was found to give good agreement in the normalization, and as such all TGLF simulations presented hereafter were run with this choice.

For the comparison we use the gyro-Bohm normalized heat-fluxes computed by TGLF,

$$\hat{Q}_{\text{TGLF}} = \frac{Q_e}{Q_{\text{GB}}}, \quad (3.12)$$

[†] These are called `cgyro` and `gene` units in the TGLF code, respectively.

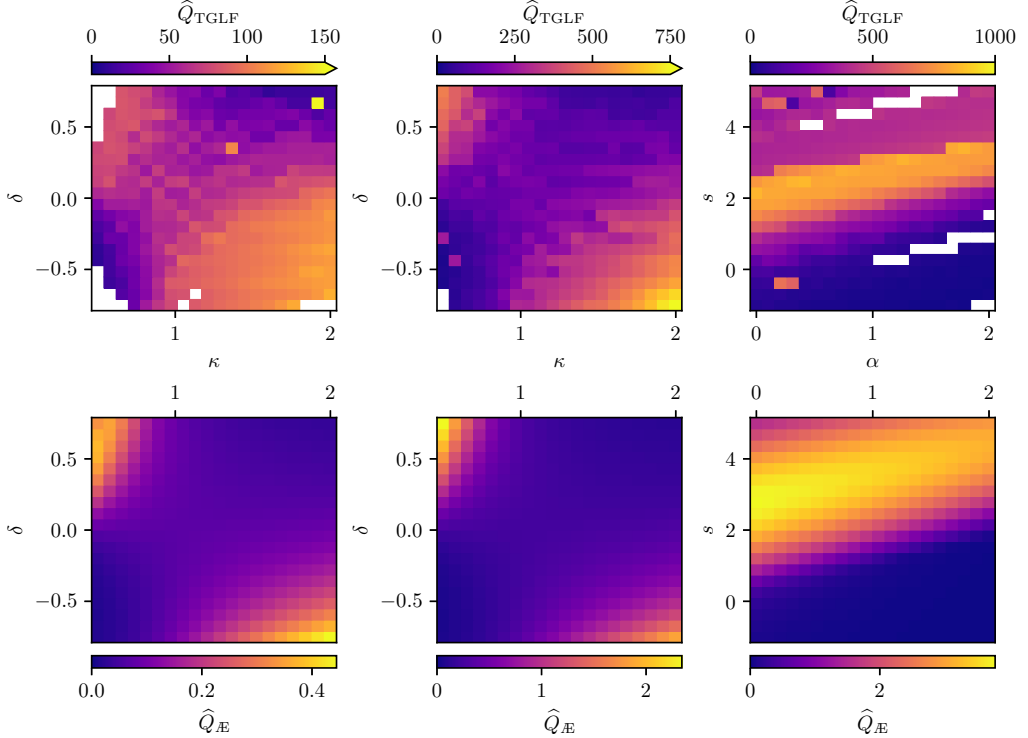


Figure 11: Comparison between codes, showing the correspondence between the estimate of the heat-flux from $\mathcal{A}E$ and TGLF. The top row displays the heat-flux from TGLF, and the bottom row displays the corresponding estimate from $\mathcal{A}E$. One can see agreement in trends, though the details differ. The left two columns have a Miller vector $[\epsilon, \kappa, \delta, s_\kappa, s_\delta, \partial_r R_0, q, s, \alpha]$ of $[1/3, \kappa, \delta, 0, 0, 0, 2, s, 0]$, and the right-most column has as Miller vector of $[1/3, 1, 1/2, 0, 0, 0, 2, s, \alpha]$. The first column has $\hat{\omega}_n = 3$, the second and third column have $\hat{\omega}_n = 6$, and $\eta = 1$ in all plots. The white masked out regions have a dominant instability which is not in the electron direction, and as such we filter them out.

where Q_e is the electron heat-flux from TGLF, and Q_{GB} is the gyro-Bohm heat-flux. This is compared with the estimate of the gyro-Bohm normalized heat-flux from $\mathcal{A}E$ Mackenbach *et al.* (2022, 2023b), which is

$$\hat{Q}_{\mathcal{A}E} \equiv \hat{A}^{3/2}. \quad (3.13)$$

With such a power law, a linear correlation between $Q_{\mathcal{A}E}$ and Q_e from nonlinear gyrokinetic simulations was found for pure density-gradient driven TEMs, which is different from the current comparison in which both the electron temperature and density gradient drive the TEM ($\eta = 1$). The data-points in the comparison are chosen in order to verify that TGLF reproduces trends discussed in previous sections, where we also found regions where the correspondence is worse.

A comparison in the (κ, δ) and (s, α) planes is displayed in Fig. 11. One can see that there is good correspondence in trends: decreasing the magnetic shear and/or increasing the pressure gradient helps in reducing the heat flux, and negative triangularity leads to an increase in transport for high gradients and low shear. There are however also clear differences visible between the two models for the heat flux, which are especially evident

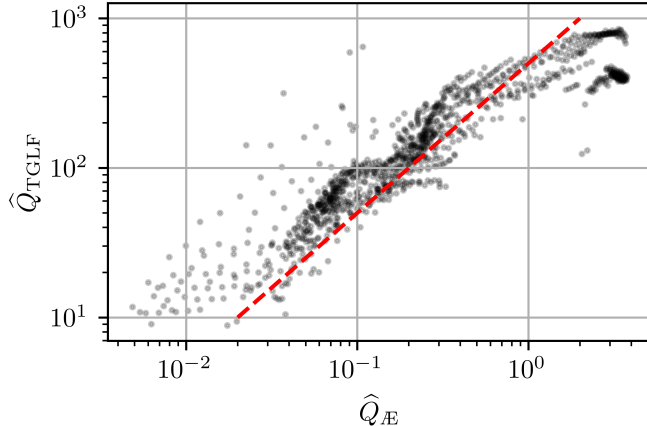


Figure 12: A scatter plot showing the relation between the two estimates of the non-linear heat-flux. The red dashed line is the expected linear relationship. The plot consists of $N = 1152$ points.

in the (s, α) -plot. A clear discrepancy can be seen at high values of shear, where the TGLF heat flux drops sharply. To further investigate this relation between the two estimates, all simulation data shown in Fig. 11 has been combined in a scatter plot shown in Fig. 12. Here we see that there is a linear correlation for most of the data, though there exists data-points that deviate more significantly from the linear relationship. There are various reasons why such a discrepancy may occur:

- There may be other instabilities present which are not captured by the AE of trapped electrons, such as the ubiquitous mode or the universal instability (Landreman *et al.* 2015; Helander & Plunk 2015). More generally, if there are instabilities present which do not derive their energy from trapped electrons, the current AE -model is no longer expected to be an accurate measure.
- The AE length-scale C_r may vary more significantly for certain choices of equilibrium parameters, and choosing $C_r = 1$ is then a poor approximation.
- Perhaps the choice of B_{ref} is not ideal: there may be more suitable choices of a reference field resulting in better correspondence (though this could formally be absorbed into C_r).
- The AE can be interpreted as an upper bound on the free energy of a plasma. A significant portion of the free energy may reside in the zonal flow, which acts stabilising, and the AE does not account for this. If the fraction of the AE which resides in the zonal flow changes significantly, one could reasonably expect that AE ceases to be an accurate measure.
- The TGLF's quasilinear saturated fluxes in both the (κ, δ) and (s, α) planes show occasional extreme outliers for small changes in input. Although TGLF has been extensively verified against a wide variety of nonlinear gyrokinetic simulations, the regime explored in this work is not the typical input space and might require separate verification.

A future investigation could, perhaps, find a fitting function for C_r such that the error in the estimated transport is minimal. However, seeing that general trends are well captured by AE , it may already serve as a useful estimate for transport at low computational cost (AE calculations are roughly a factor 50 faster than the presented TGLF calculations).

4. Conclusions

We have shown that it is possible to simplify the analytical expression for the $\mathcal{A}E$ of trapped electrons in the case of an omnigenous system, which speeds up calculations. If one furthermore employs an analytical local solution to the Grad-Shafranov equation, explicit expression of various quantities needed in the calculation of the $\mathcal{A}E$ (e.g., bounce-averaged drifts, bounce times) can be found as in Roach *et al.* (1995). Making use of an equilibrium parameterisation proposed by Miller *et al.* (1998), we go on to investigate how $\mathcal{A}E$ depends on these equilibrium parameters. Using this set-up, we observe several interesting features of the $\mathcal{A}E$:

- (i) Increasing the magnetic shear or the Shafranov shift tends to be stabilising as indicated by a reduction in the $\mathcal{A}E$, and these trends hold for many different choices of geometry.
- (ii) Negative triangularity can be stabilising, particularly in configurations with significant positive shear or small gradients, but not always.
- (iii) The $\mathcal{A}E$ has different scalings with respect to the gradient strength in weakly and strongly driven regimes. We employ this difference in scaling to estimate a gradient-threshold like quantity, and we find that it has similar behaviours as found in critical-gradient literature; an increase in shear tends to increase this gradient-threshold and negative triangularity benefits from an especially high gradient-threshold.
- (iv) Using $\mathcal{A}E$ for shape-optimisation we show that the optimal solution is strongly dependent on density gradients, temperature gradients, and magnetic shear, implying that the optimisation is sensitive to the density, pressure, and q -profiles.
- (v) One investigation is presented on how the $\mathcal{A}E$ varies as one consistently increases the density and pressure gradient, whilst decreasing the shear. We find that in such scenarios one can find solutions with large gradients yet low $\mathcal{A}E$. Such solutions tend to exist for positive triangularity tokamaks but not for negative triangularity tokamaks.
- (vi) A comparison is made between $\mathcal{A}E$ and TGLF. We observe fairly good correlation between the heat-flux and $A^{3/2}$, indicating that $\mathcal{A}E$ can be a useful measure for tokamak transport.

The results suggest that various observed trends regarding turbulent transport in tokamaks may partly be understood in terms of $\mathcal{A}E$, which has a simple physical interpretation and is cheap to compute. The analytical framework can readily be extended to account for an equilibrium model which allows for other shaping and plasma parameters such as plasma rotation (Hameiri 1983; Miller *et al.* 1995), squareness (Turnbull *et al.* 1999), and up-down asymmetry (Rodrigues & Coroado 2018), though no such investigation is presented here.

Acknowledgments

We wish to thank J.M. Duff, R. Wolf, A. Goodman, P. Mulholland, P. Costello, M.J. Pueschel, F. Jenko, and E. Rodriguez for insightful discussions. This work was partly supported by a grant from the Simons Foundation (560651, PH), and this publication is part of the project “Shaping turbulence—building a framework for turbulence optimisation of fusion reactors,” with Project No. OCENW.KLEIN.013 of the research program “NWO Open Competition Domain Science” which is financed by the Dutch Research Council (NWO). This work has been carried out within the framework of the EUROfusion Consortium, funded by the European Union via the Euratom Research and Training Program (Grant Agreement No. 101052200—EUROfusion). Views and opinions expressed are however those of the author(s) only and do not necessarily reflect those of the European Union or

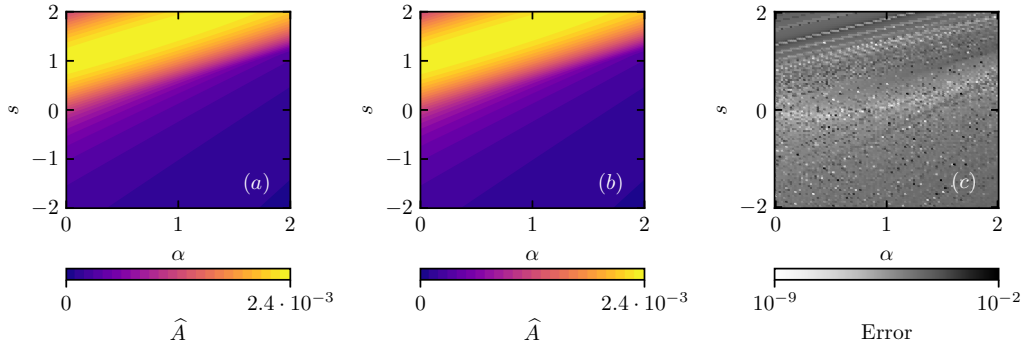


Figure 13: Comparison of the \mathcal{AE} as calculated with two different codes. Plot (a) is calculated using the $s\text{-}\alpha$ routine, and (b) is calculated using the Miller code. The plots are visually indistinguishable. Calculated using $q = 2$, $\epsilon = 10^{-6}$, $\hat{\omega}_n = 3$, and $\eta = 1$. All other parameters for Miller are set to zero, as required in the limit of the $s\text{-}\alpha$ tokamak. Plot (c) showcases the relative error, where it can be seen that the relative error is very small for large regions of $s\text{-}\alpha$ space. Note that the colourbar scale in plot (c) is logarithmic.

the European Commission. Neither the European Union nor the European Commission can be held responsible for them.

Competing interests

The authors declare no competing interests.

Appendix A. Comparison between circular tokamak and Miller code

Here we show that the two codes which calculate the \mathcal{AE} in both the circular $s\text{-}\alpha$ tokamak, for which the equation is given in (2.63), and a Miller tokamak, as given in Eq. (2.44), indeed yield the same results in the limit of a large aspect ratio circular tokamak. For a proper comparison, we set the Miller parameters such that one approaches the $s\text{-}\alpha$ limit. As such, we choose $\epsilon = 10^{-6}$, $q = 2$, and all other Miller components of the Miller vector as given in (2.50) are set to zero. There is one numerical parameter of interest in the Miller code, the number of θ points which are used to evaluate the bounce integrals of Eq. (2.37) using a generalized trapezoidal method (Mackenbach *et al.* 2023a). In the comparison presented here we use 10^3 equidistant nodes for θ . The integral over the pitch angle is done using quadrature methods.

The comparison is shown in Fig. 13. In this figure, three different contour plots are shown; (a) is the available energy as calculated from Eq. (2.63). Plot (b) shows the result as calculated from Eq. (2.44). Finally, plot (c) shows the relative error between the two codes (more precisely, it is the difference between plot (a) and (b), divided by plot (a)). It can be seen that the error is typically quite small, with a maximal value of 1% and a mean value of 0.004%. If one chooses different parameters (safety factor, density gradient, or η) the error remains similarly small.

All plots presented in the current publication are generated using the same or even more refined numerical parameters as used here, so that we have a fairly high degree of confidence that the presented trends are indeed physical and not numerical. Further convergence checks (increasing the resolution of θ and adjusting tolerances of the quadra-

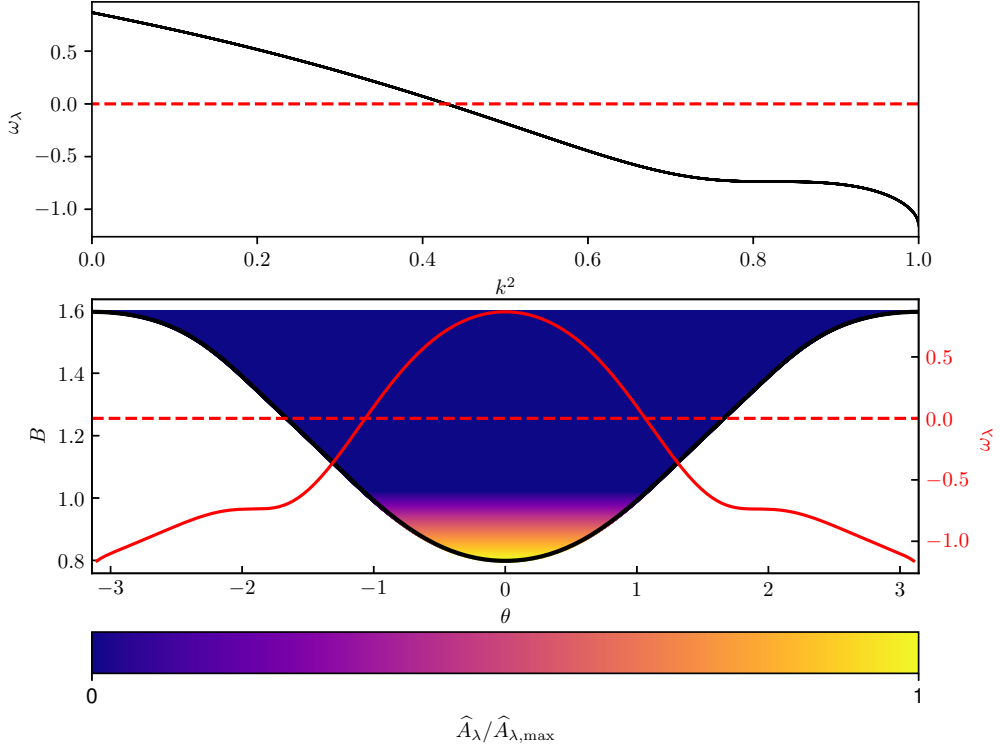


Figure 14: The precession frequency and $\mathcal{A}\mathcal{E}$ distribution for a positive triangularity tokamak

ture methods) do not alter the plots presented in this publication in a visually discernible manner.

Appendix B. Negative triangularity and trapped particle precession

In this section, we investigate the difference in trapped particle orbits in positive and negative triangularity tokamaks. To this end, we investigate the dependence of Eq. (2.37) on δ , and we set the other components of the Miller vector equal to $[\epsilon, \kappa, \delta, s_\kappa, s_\delta, \partial_r R_0, q, s, \alpha] = [1/3, 2, \delta, 0, 0, 0, 2, 0, 0]$.

The result for a positive triangularity tokamak ($\delta = 0.5$) is plotted in Fig. 14, where we have plotted ω_λ as a function of its bounce points θ , which satisfy

$$1 - \lambda \hat{B}(\theta) = 0. \quad (\text{B1})$$

We have furthermore displayed the $\mathcal{A}\mathcal{E}$ per λ , called \hat{A}_λ , which is the integrand of Eq. (2.44). This is done by coloring a line of constant λ (which corresponds to constant B) according to its A_λ . Finally, we also display ω_λ as a function of the trapping parameter k^2 which maps $\lambda \mapsto [0, 1]$ according to

$$k^2 = \frac{\hat{B}_{\max} - \lambda \hat{B}_{\max} \hat{B}_{\min}}{\hat{B}_{\max} - \hat{B}_{\min}}, \quad (\text{B2})$$

where the subscripts max and min refer to the maximal and minimal values of the functions respectively. With this convention, $k^2 = 0$ corresponds to the most deeply trapped

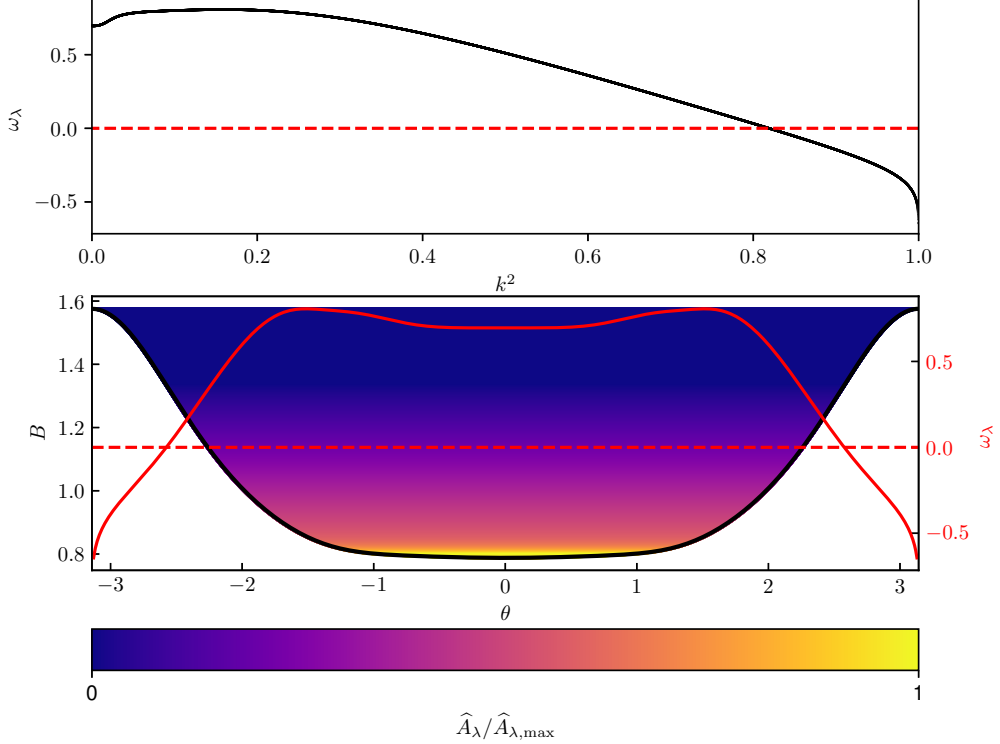


Figure 15: The precession frequency and \mathcal{AE} distribution for a negative triangularity tokamak

particles and $k^2 = 1$ to the most shallowly trapped particles. We have furthermore included a red dashed line, which delineates where ω_λ changes sign, which determines stability in a purely density-gradient-driven TEM. In the figure, $\omega_\lambda > 0$ corresponds to instability (and associated \mathcal{AE}). It can be seen that this positive triangularity tokamak is unstable up to roughly $k^2 = 1/2$, and the magnetic well is relatively narrow

The same information is displayed for a tokamak which has $\delta = -0.5$ in Fig. 15. It can be seen that the precession frequencies are unstable for a broader range of values for k^2 . The \mathcal{AE} is furthermore weighted by the bounce-time of a particle, which can become very large at the bottom of a magnetic well in a negative triangularity tokamak. As such, the negative triangularity case (with the Miller vectors as chosen here) has *higher* \mathcal{AE} than the positive triangularity case.

From numerical experiments, we find that an important term in determining the sign of ω_λ in these cases is \hat{R}_c in Eq. (2.37). As such, we postulate that, although the bounce points are in regions of “good curvature”, the curvature drive for the trapped particle precession is significantly different in positive and negative triangularity tokamaks. The particles which experience curvature drive in negative triangularity tokamaks are importantly the deeply trapped particles, which tend to be most unstable against the TEM with a density gradient. This is in contrast to positive triangularity tokamaks, where the most shallowly trapped particles experience significant curvature drive. These shallowly trapped particles however, are stabilised by the fact that they experience an averaged drift, and as such the curvature drive here is less deleterious. A graphical illustration of this is given in Fig. 16. As in previous comparisons, this result can change non-trivially

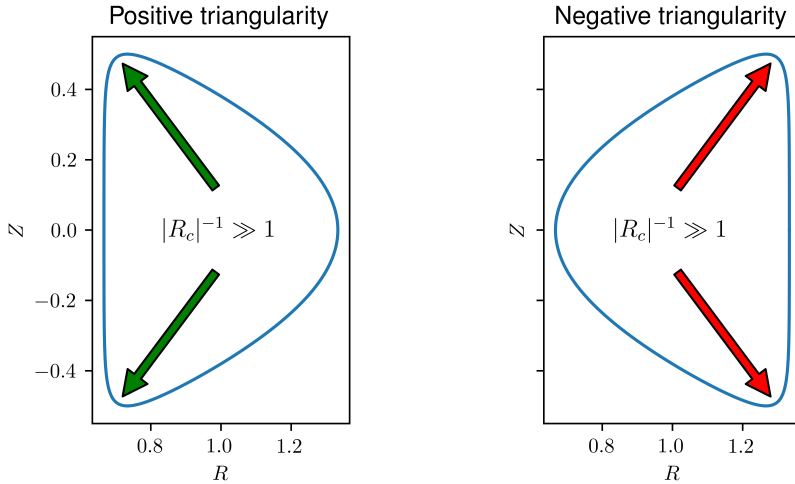


Figure 16: Comparison highlighting the difference in curvature drive for the different classes of particles. Positive triangularity tends to have shallowly trapped particles which experience significant curvature drive, where the negative triangularity case has deeply trapped particles experiencing curvature drive.

when changing the Miller vector. Note that such an explanation also highlights why these trends tend to invert for tokamaks which have $\kappa < 1$. When the elongation is less than unity, the sharpest angle (corresponding to large R_c^{-1}) is on the outboard-side in a positive triangularity tokamak, and on the inboard side for a negative triangularity tokamak. As such, when $\kappa < 1$ and $\delta > 0$ the most deeply trapped particles experience much curvature drive, destabilising the TEM. This is in contrast to $\kappa < 1$ and $\delta < 0$ which has the shallowly trapped particles experiencing much curvature drive, which would benefit from the averaging effect of the drift.

REFERENCES

- C. MERCIER & N. LUC 1974 Report No. EUR-5127e 140 (Commission of the European Communities, Brussels, 1974). *Tech. Rep..*
- CONNOR, J W, HASTIE, R J & MARTIN, T J 1983 Effect of pressure gradients on the bounce-averaged particle drifts in a tokamak. *Nucl. Fusion* **23** (12), 1702.
- COPPI, B & PEGORARO, F 1977 Theory of the ubiquitous mode. *Nuclear Fusion* **17** (5), 969.
- DAGAZIAN, R Y & PARIS, R B 1982 The effects of high shear on ideal ballooning. *Plasma Physics* **24** (6), 661–670.
- DIMITS, A M, BATEMAN, G, BEER, M A, COHEN, B I, DORLAND, W, HAMMETT, G W, KIM, C, KINSEY, J E, KOTSCHEKREUTHER, M, KRITZ, A H, LAO, L L, MANDREKAS, J, NEVINS, W M, PARKER, S E, REDD, A J, SHUMAKER, D E, SYDORA, R & WEILAND, J 2000 Comparisons and physics basis of tokamak transport models and turbulence simulations. *Phys. Plasmas* **7** (3), 969–983.
- ENDRES, STEFAN C, SANDROCK, CARL & FOCKE, WALTER W 2018 A simplicial homology algorithm for Lipschitz optimisation. *Journal of Global Optimization* **72** (2), 181–217.
- GARDNER, CLIFFORD S 1963 Bound on the energy available from a plasma. *Phys. Fluids* **6** (6), 839–840.
- HAMEIRI, ELIEZER 1983 The equilibrium and stability of rotating plasmas. *The Physics of Fluids* **26** (1), 230–237.

- HELANDER, PER 2017 Available energy and ground states of collisionless plasmas. *J. Plasma Phys.* **83** (4).
- HELANDER, PER 2020 Available energy of magnetically confined plasmas. *J. Plasma Phys.* **86** (2).
- HELANDER, P & PLUNK, GG 2015 The universal instability in general geometry. *Physics of Plasmas* **22** (9).
- HELANDER, PER & SIGMAR, DIETER J 2005 *Collisional transport in magnetized plasmas*. Cambridge university press.
- JENKO, F, DORLAND, W & HAMMETT, GW 2001 Critical gradient formula for toroidal electron temperature gradient modes. *Physics of Plasmas* **8** (9), 4096–4104.
- KESNER, J, RAMOS, J J & GANG, F Y. 1995 Comet cross-section tokamaks. *Journal of Fusion Energy* **14** (4), 361–371.
- KESSEL, C, MANICKAM, JF, REWOLDT, G & TANG, W M 1994 Improved plasma performance in tokamaks with negative magnetic shear. *Phys. Rev. Lett.* **72** (8), 1212.
- KINSEY, J E, WALTZ, R E & CANDY, J 2006 The effect of safety factor and magnetic shear on turbulent transport in nonlinear gyrokinetic simulations. *Phys. Plasmas* **13** (2), 022305.
- KOLMES, EJ & FISCH, NJ 2022 Minimum stabilizing energy release for mixing processes. *Physical Review E* **106** (5), 055209.
- KOLMES, E J & FISCH, N J 2020 Recovering Gardner restacking with purely diffusive operations. *Phys. Rev. E* **102** (6), 63209.
- KOLMES, E J, HELANDER, P & FISCH, N J 2020 Available energy from diffusive and reversible phase space rearrangements. *Phys. Plasmas* **27** (6), 062110.
- LANDREMAN, MATT, ANTONSEN JR, THOMAS M & DORLAND, WILLIAM 2015 Universal instability for wavelengths below the ion larmor scale. *Physical review letters* **114** (9), 095003.
- MACKENBACH, RJJ, DUFF, JM, GERARD, MJ, PROLL, JHE & HELANDER, P 2023a Equivalent definitions, numerical implementations, and example cases .
- MACKENBACH, R J J, PROLL, JOSEFINE H E & HELANDER, P 2022 Available Energy of Trapped Electrons and Its Relation to Turbulent Transport. *Physical Review Letters* **128** (17), 175001.
- MACKENBACH, R J J, PROLL, JOSEFINE H E & HELANDER, P 2023b The available energy of trapped electrons, its distribution across bounce wells, and its relation to turbulent transport (To be published)). *Journal of Plasma Physics* .
- MARINONI, A, AUSTIN, M E, HYATT, A W, WALKER, M L, CANDY, J, CHRYSTAL, C, LASNIER, C J, MCKEE, G R, ODSTRČIL, T, PETTY, C C, PORKOLAB, M, ROST, J C, SAUTER, O, SMITH, S P, STAEBLER, G M, SUNG, C, THOME, K E, TURNBULL, A D & ZENG, L 2019 H-mode grade confinement in L-mode edge plasmas at negative triangularity on DIII-D. *Physics of Plasmas* **26** (4), 042515.
- MERLO, G, BRUNNER, S, SAUTER, OLIVIER, CAMENEN, Y, GÖRLER, T, JENKO, F, MARINONI, A, TOLD, D & VILLARD, LAURENT 2015 Investigating profile stiffness and critical gradients in shaped TCV discharges using local gyrokinetic simulations of turbulent transport. *Plasma Phys. Control. Fusion* **57** (5), 054010.
- MERLO, G, FONTANA, MATTEO, CODA, STEPHANO, HATCH, D, JANHUNEN, S, PORTE, LAURIE & JENKO, F 2019 Turbulent transport in tcv plasmas with positive and negative triangularity. *Physics of Plasmas* **26** (10), 102302.
- MERLO, G, HUANG, Z, MARINI, C, BRUNNER, S, CODA, S, HATCH, D, JAREMA, D, JENKO, F, SAUTER, O & VILLARD, L 2021 Nonlocal effects in negative triangularity TCV plasmas. *Plasma Phys. Control. Fusion* **63** (4), 044001.
- MERLO, GABRIELE & JENKO, FRANK 2023 Interplay between magnetic shear and triangularity in ion temperature gradient and trapped electron mode dominated plasmas. *Journal of Plasma Physics* **89** (1), 905890104.
- MILLER, R L, CHU, M S, DOMINGUEZ, R R & OHKAWA, T 1989 Maximum J tokamak by plasma shaping. *Comments on Plasma Physics and Controlled Fusion* **12** (3), 125–132.
- MILLER, R L, CHU, MING-SHENG, GREENE, J M, LIN-LIU, Y R & WALTZ, R E 1998 Noncircular, finite aspect ratio, local equilibrium model. *Physics of Plasmas* **5** (4), 973–978.

- MILLER, R L, WAELBROECK, F L, HASSAM, A B & WALTZ, R E 1995 Stabilization of ballooning modes with sheared toroidal rotation. *Physics of Plasmas* **2** (10), 3676–3684.
- MIYAMOTO, KENRO 2005 *Plasma physics and controlled nuclear fusion*, , vol. 38. Springer Science & Business Media.
- NELSON, ANDREW OAKLEIGH, PAZ-SOLDAN, CARLOS & SAARELMA, SAMULI 2022 Prospects for H-mode inhibition in negative triangularity tokamak reactor plasmas. *Nuclear Fusion*
- PROLL, J.H.E., PLUNK, G.G., FABER, B.J., GÖRLER, T., HELANDER, P., MCKINNEY, I.J., PUESCHEL, M.J., SMITH, H.M. & XANTHOPOULOS, P. 2022 Turbulence mitigation in maximum-j stellarators with electron-density gradient. *Journal of Plasma Physics* **88** (1), 905880112.
- RETTIG, C L, PEEBLES, W A, DOYLE, E J, BURRELL, K H, GREENFIELD, C, STAEBLER, G M & RICE, B W 1997 Microturbulence reduction during negative central shear tokamak discharges. *Phys. Plasmas* **4** (11), 4009–4016.
- ROACH, C M, CONNOR, J W & JANJUA, S 1995 Trapped particle precession in advanced tokamaks. *Plasma Phys. Control. Fusion* **37** (6), 679.
- RODRIGUES, PAULO & COROADO, ANDRÉ 2018 Local updown asymmetrically shaped equilibrium model for tokamak plasmas. *Nuclear Fusion* **58** (10), 106040.
- SAARELMA, SAMULI, AUSTIN, MAX E, KNOLKER, M, MARINONI, ALESSANDRO, PAZ-SOLDAN, CARLOS, SCHMITZ, LOTHAR & SNYDER, PHILIP B 2021 Ballooning instability preventing the H-mode access in plasmas with negative triangularity shape on the DIII-D tokamak. *Plasma Physics and Controlled Fusion* **63** (10), 105006.
- STAEBLER, GM & KINSEY, JE 2010 Electron collisions in the trapped gyro-landau fluid transport model. *Physics of Plasmas* **17** (12), 122309.
- STAEBLER, GM, KINSEY, JE & WALTZ, RE 2007 A theory-based transport model with comprehensive physics. *Physics of Plasmas* **14** (5), 055909.
- STAEBLER, GARY M, BELLI, EA, CANDY, J, KINSEY, JE, DUDDING, H & PATEL, B 2021 Verification of a quasi-linear model for gyrokinetic turbulent transport. *Nuclear Fusion* **61** (11), 116007.
- STAEBLER, GARY M, CANDY, JEFFREY, BELLI, EMILY A, KINSEY, JON E, BONANOMI, N & PATEL, BHAVIN 2020 Geometry dependence of the fluctuation intensity in gyrokinetic turbulence. *Plasma Physics and Controlled Fusion* **63** (1), 015013.
- STRAIT, E J, CASPER, T A, CHU, M S, FERRON, J R, GAROFALO, A, GREENFIELD, C M, LA HAYE, R J, LAO, L L, LAZARUS, E A & MILLER, R L 1997 Stability of negative central magnetic shear discharges in the DIII-D tokamak. *Phys. Plasmas* **4** (5), 1783–1791.
- TURNBULL, A D, LIN-LIU, Y R, MILLER, R L, TAYLOR, T S & TODD, T N 1999 Improved magnetohydrodynamic stability through optimization of higher order moments in cross-section shape of tokamaks. *Physics of Plasmas* **6** (4), 1113–1116.